Galaxy cluster cores as seen with VLT/MUSE: New strong-lensing analyses of RX J2129.4 + 0009, MS 0451.6 − 0305, and MACS J2129.4 − 0741

Mathilde Jauzac [1,2,3,4,5]★ Baptiste Klein [5,6] Jean-Paul Kneib,[5,7] Johan Richard,[8] Markus Rexroth,[5] Christoph Schäfer[5] and Aurélien Verdier[5]

[1]*Centre for Extragalactic Astronomy, Durham University, South Road, Durham DH1 3LE, UK*
[2]*Institute for Computational Cosmology, Durham University, South Road, Durham DH1 3LE, UK*
[3]*Astrophysics Research Centre, University of KwaZulu-Natal, Westville Campus, Durban 4041, South Africa*
[4]*School of Mathematics, Statistics & Computer Science, University of KwaZulu-Natal, Westville Campus, Durban 4041, South Africa*
[5]*Institute of Physics, Laboratory of Astrophysics, Ecole Polytechnique Fédérale de Lausanne (EPFL), Observatoire de Sauverny, CH-1290 Versoix, Switzerland*
[6]*Sub-department of Astrophysics, Department of Physics, University of Oxford, Oxford OX1 3RH, UK*
[7]*Aix Marseille Université, CNRS, LAM (Laboratoire d'Astrophysique de Marseille) UMR 7326, F-13388 Marseille, France*
[8]*Univ Lyon, Univ Lyon1, Ens de Lyon, CNRS, Centre de Recherche Astrophysique de Lyon UMR5574, F-69230 Saint-Genis-Laval, France*

ABSTRACT

We present strong-lensing analyses of three galaxy clusters, RX J2129.4 + 0009 ($z = 0.235$), MS 0451.6 − 0305 ($z = 0.55$), and MACS J2129.4 − 0741 ($z = 0.589$), using the powerful combination of *Hubble Space Telescope* (*HST*) multiband observations, and Multi-Unit Spectroscopic Explorer (MUSE) spectroscopy. In RX J2129, we newly spectroscopically confirm 15 cluster members. Our resulting mass model uses 8 multiple image systems as we include a galaxy–galaxy lensing system north-east of the cluster, and is composed of 71 haloes including one dark matter cluster-scale halo and two galaxy-scale haloes optimized individually. For MS 0451, we report the spectroscopic identification of two new systems of multiple images in the northern region and 112 cluster members. Our mass model uses 16 multiple image systems and 146 haloes, including 2 large-scale haloes and 7 galaxy-scale haloes independently optimized. For MACS J2129, we report the spectroscopic identification of one new multiple image system at $z = 4.41$, and newly measure spectroscopic redshifts for four cluster members. Our mass model uses 14 multiple image systems, and is composed of 151 haloes, including 2 large-scale haloes and 4 galaxy-scale haloes independently optimized. Our best models have rms of 0.29, 0.6, 0.74 arcsec in the image plane for RX J2129, MS 0451, and MACS J2129, respectively. This analysis presents a detailed comparison with the existing literature showing excellent agreements, and discuss specific studies of lensed galaxies, e.g. a group of submillimetre galaxies at $z = 2.9$ in MS 0451, and a bright $z = 2.1472$ red singly imaged galaxy in MACS J2129.

Key words: gravitational lensing: strong – Techniques: imaging spectroscopy – Galaxies: clusters: general – Galaxies: clusters: individual (RX J2129.4 + 0009, MS 0451.6 − 0305, MACS J2129.4 − 0741).

1 INTRODUCTION

Clusters of galaxies are the most spectacular strong lenses in the Universe. Due to the high-mass density in their cores, it is not uncommon to observe giant arcs and multiple images of sources located behind them. This gravitational lensing effect distorts, and magnifies the light emitted by background galaxies, transforming these clusters into cosmic telescopes (for a review, see e.g. Massey, Kitching & Richard 2010; Kneib & Natarajan 2011; Hoekstra et al. 2013; Treu & Ellis 2015; Kilbinger 2015; Bartelmann & Maturi 2017). Such strong-lensing features are extremely useful to map the total mass distribution within the central regions of clusters (e.g. Richard et al. 2014; Jauzac et al. 2014; Johnson et al. 2014; Coe, Bradley & Zitrin 2015; Caminha et al. 2017b; Williams et al. 2018; Diego et al. 2018; Mahler et al. 2018; Lagattuta et al. 2019; Sharon et al. 2020). These mass models can then be used to constrain the physics of Dark Matter,

such as its self-interaction cross-section (see Harvey et al. 2014, 2015; Wittman, Golovich & Dawson 2018), or test the cosmological paradigm (e.g. Jullo et al. 2010a; Acebron et al. 2017; Natarajan et al. 2017; Jauzac et al. 2018), but also to probe the early Universe and thus the epoch of reionization (e.g. Atek et al. 2015; Bouwens et al. 2017; Livermore, Finkelstein & Lotz 2017; Atek et al. 2018; Ishigaki et al. 2018). Hence, the need to have accurate and precise mass models for a large number of galaxy clusters.

Over the past two decades, the precision of strong-lensing mass modeling of galaxy clusters has dramatically increased. This is mainly due to the combination of powerful post-processing algorithms and high resolution imaging. On the one hand, the use of the Markov Chain Monte Carlo (MCMC) sampling of the parameter space in the Bayesian framework allowed for robust estimations of the most likely mass models for a given set of constraints (e.g. our team uses LENSTOOL which is presented in Kneib et al. 1996; Jullo et al. 2007, 2010b; Niemiec et al. 2020). On the other hand, the quality of observations with the *Hubble Space Telescope* (*HST*)

provided astronomers with the deepest and highest resolution images of strong-lensing clusters (e.g. Postman et al. 2012; Schmidt et al. 2014; Treu et al. 2015; Lotz et al. 2017; Steinhardt et al. 2020, see also the webpages of *Hubble* Frontier Fields,[1] GLASS,[2] RELICS[3], and BUFFALO[4] surveys). This resulted in mass models with an unrivalled precision for numerous galaxy clusters (e.g. Zitrin et al. 2011b; Richard et al. 2014; Johnson et al. 2014; Jauzac et al. 2015; Diego et al. 2016). High-resolution imaging allows precise measurements of the location of multiple images. However, if their exact distance, i.e. their redshift, is not measured, then mass models are highly degenerate, and the resulting mass distribution is biased, hence the strong need for measurements of spectroscopic redshifts ($\Delta z < 0.01$, see Lagattuta et al. 2017; Richard et al. 2015; Grillo et al. 2016; Jauzac et al. 2016a, 2019; Mahler et al. 2018, 2019; Lagattuta et al. 2019; Remolina González, Sharon & Mahler 2018). As shown in Johnson & Sharon (2016), Cerny et al. (2018), and Remolina González et al. (2018), the spectroscopic redshift information is mandatory in order to obtain precise strong-lensing mass models.

The Multi-Unit Spectroscopic Explorer (MUSE; Bacon et al. 2010) is a second-generation integral field spectrograph at the Very Large Telescope (VLT). MUSE large field of view of 1 arcmin^2 is perfectly adapted to the observation of the core of galaxy clusters (Richard et al. 2015, 2021; Grillo et al. 2016; Caminha et al. 2017a,b; Chirivì et al. 2018; Rescigno et al. 2020), where most multiple images are likely to be observed (e.g. Kneib & Natarajan 2011). Its high sensitivity between 4750 Å and 9350 Å enables the detection of sources with redshifts up to $z = 6$ (Bacon et al. 2015). Over the past 6 years, strong cluster lenses have been commonly observed with MUSE, leading to the measurement of spectroscopic redshifts for multiple images, their multiplicity confirmation, as well as the identification of new multiple image systems which are not even detected in *HST* observations (e.g. Richard et al. 2015; Jauzac et al. 2016a; Caminha et al. 2017a, 2019; Lagattuta et al. 2019).

In this paper, we present MUSE observations, and their subsequent strong-lensing analyses, for three well-known galaxy clusters: RX J2129.4 + 0009, MS 0451.6 − 0305, and MACS J2129.4 − 0741. These clusters have been observed with *HST*, and already have strong-lensing mass models published in the literature (more details are given bellow, but e.g. Richard et al. 2010; Zitrin et al. 2011b, 2015; MacKenzie et al. 2014; Monna et al. 2017; Caminha et al. 2019) which are used as references in this analysis, and referred to as *fiducial models* in the rest of the paper).

(i) RX J2129.4 + 0009 ($z = 0.235$, RX J2129 hereafter) was observed as part of the CLASH survey, and was first modelled with LENSTOOL for the Local Cluster Substructure Survey (LoCuSS, PI: G. P. Smith, see Richard et al. 2010). This model relied on a single system of multiple images which redshift was updated by Belli et al. (2013). Then, Zitrin et al. (2015) published a model which uses four multiple image systems, two being spectroscopically confirmed. Desprez et al. (2018) presented a revised model, including one galaxy–galaxy lensing system located ∼80 arcsec from the cluster centre, in the vicinity of an isolated cluster galaxy. Finally, Caminha et al. (2019) presented a strong-lensing mass model which takes advantage of the MUSE observations presented in this paper.

(ii) MS 0451.6 − 0305 ($z = 0.55$ − MS 0451 hereafter) is originally known for its large brightness in the X-rays (e.g. Ellingson et al. 1998; Molnar et al. 2002; LaRoque et al. 2003; Gioia et al. 1990; Donahue et al. 2003; Geach et al. 2006), and hosts several strongly lensed submillimetric sources with radio counterparts (e.g. Takata et al. 2003; Borys et al. 2004; Berciano Alba et al. 2007, 2010; MacKenzie et al. 2014). Increasingly precise strong-lensing mass models were obtained by Borys et al. (2004), Berciano Alba et al. (2007), Zitrin et al. (2011b), and most recently by MacKenzie et al. (2014), where they included sub-millimetre detections. The latter relies on 8 multiple image systems located in the south of the cluster, leaving the north poorly constrained. However, more recent imaging with *HST*, and spectroscopy with VLT/X-Shooter and Keck/LRIS, allowed the identification of 8 new multiple image systems, including a quintuple image at redshift $z = 6.7$ in the north (Knudsen et al. 2016; Richard et al. in preparation). The giant arc identified in Borys et al. (2004), and the system at redshift $z = 6.7$, are the only multiple image systems with confirmed spectroscopic redshifts.

(iii) MACS J2129.4 − 0741 ($z = 0.589$ − MACS J2129 hereafter; Ebeling et al. 2007) is part of the Cluster Lensing And Supernova survey with *Hubble* (CLASH; Postman et al. 2012). It was modelled by Zitrin et al. (2011a) and more recently by Monna et al. (2017) using CLASH photometry (Zitrin et al. 2015), and VLT-VIMOS spectroscopic data (Rosati et al. 2014). Among the 9 multiple image systems used in the mass model presented by Monna et al. (2017), two systems are not spectroscopically confirmed. Then, Caminha et al. (2019) presented a strong-lensing model using LENSTOOL, which takes advantage of the MUSE observations presented in this work.

This paper is organized as follows. Section 2 presents the details of the pipeline used to extract the spectra from the MUSE datacubes. Section 2.4 describes redshift measurements, and presents our results for the three galaxy clusters. Section 3 details the strong-lensing mass models of RX J2129, MS 0451, and MACS J2129. Section 4 presents our results and discusses them with regards to previous strong-lensing analyses of these clusters. We finally conclude in Section 5. Throughout the paper, we assume a standard cosmological model with $\Omega_M = 0.3$, $\Omega_\Lambda = 0.7$, and $H_0 = 70 \, \mathrm{km \, s^{-1} \, Mpc^{-1}}$. At the redshift of RX J2129 ($z = 0.235$), 1 arcsec covers a physical distance of 3.3734 kpc. At the redshift of MS 0451 ($z = 0.55$), 1 arcsec covers a physical distance of 6.412 kpc. Finally, for MACS J2129 ($z = 0.589$), 1 arcsec corresponds to 6.63 kpc. All magnitudes are measured using AB system.

2 MUSE OBSERVATIONS AND ANALYSIS

2.1 Observations and data reduction

RX J2129, MS 0451, and MACS J2129 were observed with MUSE on the VLT. Table 1 gives the details of the observations, including dates, pointing positions, ID, seeing conditions, and total exposure time for each data set. Observations were taken using MUSE WFM-NOAO-N mode, in good seeing conditions with full width at half maximum (FWHM) of ≈ 0.5, 0.8, and 0.9 arcsec for RX J2129, MS 0451, and MACS J2129, respectively. At each pointing, three exposures were taken, slightly shifted (by ∼0.5 arcsec) in order to mitigate systematics from the image slicer and detectors.

The data were reduced with version 1.6.4 of the standard MUSE pipeline (Weilbacher et al. 2014, 2020). We use a set of standard calibration exposures taken daily to produce bias, arcs, and flat-field master calibration files. Dark current is neglected due to its very low value with MUSE (≈ 1 electron h^{-1}; Bacon et al. 2015). We first

Table 1. Summary of MUSE observations for all three clusters. Columns 1–3 indicate, respectively, the name of the cluster, its average redshift, and the ID of the ESO programme (PI: Kneib for all observations). For each pointing, we give the observation date in column 4, the total exposure time in column 5, the right ascension (R A), and declination (Decl.) of the centre of the field of view in columns 6 and 7, and the FWHM of the seeing during the observations in column 8.

Cluster	z	ESO programme	Observation date	Exposure time (s)	R A [J2000]	Decl. [J2000]	Seeing (arcsec)
RX J2129	0.235	097.A-0909(A)	2016-08-05	8940	322.42149	0.09310	0.5
			2016-09-04		322.41189	0.08682	
MS 0451	0.55	096.A-0105(A)	2016-01-10	8682	73.55165	−3.01837	0.8
			2016-01-11		73.54106	−3.00965	
MACS J2129	0.589	095.A-0525(A)	2015-06-17	8772	322.36602	−7.69040	0.9
					322.35192	−7.69040	

subtract the master bias exposures from each data set, and perform an illumination correction using in combination the master flat-field, the twilight sky exposures taken at the beginning of the night, and the illumination calibration taken soon before/after the science observations. We carry out wavelength, geometrical and astrometric calibrations in order to assign the World Coordinate System (WCS) right ascension and declination, and the wavelength to each pixel of the datacube. The flux calibration is carried out using standard star observations taken at the beginning of the observing night. For each pointing, the three individual exposures are then combined into a full datacube using a single interpolation step.

We apply the ZÜRICH ATMOSPHERE PURGE (zap; Soto et al. 2016) software version 1.0, which uses a principal components analysis to analyse objects-free regions in the datacube and subtract systematics due to sky subtraction residuals. To create the ZAP objects mask, we use the segmentation map obtained by applying the SEXTRACTOR software (Bertin & Arnouts 1996) on a white-light image collapsing the datacube along its wavelength axis.

The wavelength range of the final datacube stretches from 4750 to 9350 Å in steps of 1.25 Å, and the spaxel size is 0.2 arcsec.

2.2 Spectrum extraction

We combine MUSE observations with high-resolution images from *HST* to detect small and faint sources that remain invisible in the image obtained when the MUSE datacube is collapsed along the wavelength axis. This combination was notably used by Bacon et al. (2015, 2017) for the analysis of MUSE observations of the *Hubble* Deep Field South.

For MACS J2129 and RX J2129, we use *HST* data obtained with the *Advanced Camera for Surveys* (ACS; Ford et al. 2003) as part of the CLASH survey in the F475W, F625W, and F814W pass-bands. We also use imaging by the *Wide Field Camera 3* (WFC3) in the F110W and F160W pass-bands to cover a larger wavelength range for the source identification. For MS 0451, we use the *HST* data available in the MAST website.[5] We present in Tables 2–4, a summary of the *HST* observations used for this work for RX J2129, MS 0451, and MACS J2129, respectively, including the observation ID, the PI, the exposure time, and the observational date. For all three clusters, we applied standard data-reduction procedures. We used *HST*CAL and the most recent calibration files. The co-addition of individual frames was done using ASTRODRIZZLE after registration to a common reference image using TWEAKREG. After an iterative process, we achieve an alignment accuracy of 0.1 pixel. Our final stacked images have a pixel size of 0.03 arcsec.

[5] http://archive.stsci.edu/

Table 2. Summary of the *HST* observations used in this analysis to carry out the source identifications for RX J2129. In the context of the CLASH survey (Proposal ID 12457), observations in the UV were also carried but we do not list them as they are not used in this analysis.

Band	PID	P I	Exp. time (s)	Obs. date
ACS/F435W	12457	Postman	1023	2012-05-31
	–	–	932	2012-06-30
ACS/F475W	–	–	932	2012-05-23
	–	–	932	2012-07-09
ACS/F606W	–	–	1003	2012-05-01
	–	–	932	2012-06-12
ACS/F625W	–	–	932	2012-04-03
	–	–	932	2012-05-23
ACS/F775W	–	–	932	2012-05-01
	–	–	1018	2012-05-23
ACS/F814W	–	–	932	2012-05-31
	–	–	989	2012-06-12
	–	–	1022	2012-06-30
	–	–	990	2012-07-20
ACS/F850LP	–	–	1022	2012-04-03
	–	–	1022	2012-05-23
	–	–	1006	2012-07-09
	–	–	932	2012-07-20
	12461	Reiss	1780	2012-07-23
	–	–	1780	2012-07-30
WFC3/F105W	12457	Postman	1206	2012-05-31
	–	–	1006	2012-06-13
WFC3/F110W	–	–	1409	2012-05-23
	–	–	1006	2012-07-20
WFC3/F125W	–	–	1409	2012-04-03
	–	–	1006	2012-06-27
	–	–	1006	2012-07-09
WFC3/F140W	–	–	1306	2012-05-31
	–	–	1006	2012-06-13
WFC3/F160W	–	–	1006	2012-04-03
	–	–	1006	2012-05-23
	–	–	1409	2012-06-27
	–	–	1409	2012-07-09

We use the IFS-REDEX software to align the datacubes with the corresponding *HST* high-resolution images (Rexroth et al. 2017). We then run SEXTRACTOR on the *HST/ACS* F814W pass-band image for each cluster to automatically measure the position and FWHM of the sources in the MUSE field of view. IFS-REDEX uses the catalogue of detected sources to extract the signal in the datacube within a circle of radius 3–5 pixels according to the FWHM measurement. Sources with FWHM < 2 pixels are considered spurious detections, and are rejected.

Table 3. Summary of the *HST* observations used in this analysis to carry out the source identifications for MS 0451.

Band	PID	P I	Exp. time (s)	Obs. date
ACS/F555W	9722	Ebeling	4410	2002-01-15
ACS/F775W	9292	Ford	2440	2002-04-09
ACS/F814W	9836	Ellis	2036	2004-01-27
	10493	Gal-Yam	2162	2005-07-31
	11591	Kneib	7240	2011-02-07
ACS/F850LP	9292	Ford	2560	2002-04-10
WFC3/F110W	11591	Kneib	2612	2010-01-13
WFC3/F160W	–	–	2412	2010-01-13

In order to maximize the number of extracted spectra, we carry out a blind search in the datacube using MUSELET.[6] This software is part of the MUSE PYTHON DATA ANALYSIS FRAMEWORK (MPDAF; Bacon et al. 2016). It builds a new datacube, the narrow-band datacube, within which each wavelength plane is the mean of the 5 closest wavelength planes in the science datacube. MUSELET then uses SEXTRACTOR to extract a catalogue of sources at each wavelength in the narrow-band datacube. The latter are finally merged and sorted, providing a continuum and a single line emission catalogues.

Finally, all catalogues are merged to provide a master catalogue, which is then displayed on the high resolution image so that the user can determine whether MUSELET and SEXTRACTOR detections are matching the same source. This results in a set of spectra that we then analyse to measure the associated redshifts.

2.3 Redshift measurements

IFS-REDEX has an interactive interface that displays each extracted spectrum and its corresponding source in SAODS9 (Joye & Mandel 2003). It allows the user to modify the source redshift to match the position of an emission/absorption line template to its most likely position in the spectrum. (The template contains ∼60 lines including notably Ly α, [O II], [O III], and H β emission lines, and Ca H&K, Mg, Fe, and Na absorption lines.) To simplify the redshift identification, it is possible to smooth the signal with a Gaussian filter, and then perform a wavelet-based spectrum cleaning (Rexroth et al. 2017). The systematic error is calculated by quadratically adding the wavelength calibration error provided by the MUSE data reduction pipeline, and the error given by fitting a Gaussian to the most prominent line in the spectrum. For each redshift, we assign a quality flag (QF) of 3 if the redshift is secure, 2 if likely (e.g. only one characteristic line – for example the [O II] doublet or Ly α line with consistent photometric redshift), 1 if insecure, and 0 otherwise, i.e. in case of visually flat continuum or highly polluted spectrum.

We sequentially analyse all spectra extracted from the MUSE datacubes of the three clusters using the aforementioned method. The measured redshifts are sorted depending on whether they belong to a source located in the foreground of the cluster, in the cluster, or in the background.

2.4 Results of the redshift extraction

Fig. 1 shows the distribution of redshifts for the extracted sources for RX J2129, MS 0451, and MACS J2129. Lists of the extracted redshifts with QF larger than 2 are given in Appendix A, where Tables

[6]http://mpdaf.readthedocs.io/en/latest/muselet.html

Table 4. Summary of the *HST* observations used in this analysis to carry out the source identifications for MACS J2129. In the context of the CLASH survey (PID 12100), observations in the UV were also carried out but we do not list them as they are not used for this analysis.

Band	PID	P I	Exp. time (s)	Obs. date
ACS/F435W	12100	Postman	932	2011-07-14
ACS/F475W	–	–	1110	2011-06-03
	–	–	1110	2011-07-14
ACS/F555W	9722	Ebeling	4440	2003-09-11
ACS/F606W	12100	Postman	932	2011-05-15
	–	–	932	2011-06-24
ACS/F625W	–	–	932	2011-05-16
	–	–	991	2011-06-24
ACS/F775W	–	–	1029	2011-05-16
	–	–	995	2011-07-14
ACS/F814W	9722	Ebeling	4530	2003-09-11
	10493	Gal-Yam	2168	2005-06-18
	12100	Postman	932	2011-06-24
ACS/F850LP	–	–	1020	2011-05-15
	–	–	932	2011-06-03
	–	–	1020	2011-06-24
	–	–	932	2011-07-14
WFC3/F105W	–	–	1006	2011-05-16
	–	–	1409	2011-08-03
	13459	Treu	812	2014-05-28
	–	–	356	2014-05-29
	–	–	356	2014-08-14
	–	–	812	2014-08-15
WFC3/F110W	12100	Postman	1409	2011-05-15
	–	–	1006	2011-07-20
WFC3/F125W	–	–	1409	2011-05-16
	–	–	1006	2011-08-03
WFC3/F140W	–	–	1006	2011-06-03
	–	–	1306	2011-06-24
	13459	Treu	812	2014-05-29
	–	–	1574	2014-08-14
WFC3/F160W	12100	Postman	1006	2011-05-15
	–	–	1409	2011-06-03
	–	–	1206	2011-06-24
	–	–	1409	2011-07-20

A1–A3 give the results for RX J2129, MS 0451, and MACS J2129, respectively. The redshift intervals to consider galaxies as cluster members are established using the definition given in Ma et al. (2008), combined with the criteria defined in Rexroth et al. (2017). For each cluster, we include all galaxies with a redshift flagged as secure or likely (QF = 2, 3), and which present a continuum plus characteristic absorption lines. We here only summarize the redshift extraction.

2.4.1 RX J2129

We extracted 158 sources with redshifts ranging from 0.0 to 5.53 in RX J2129. Among them, 43 are identified as cluster members with $0.2145 < z < 0.2410$, 24 as foreground objects, and 91 as background sources (i.e. total number of sources without accounting for image multiplicity).When comparing our results to those reported in Caminha et al. (2019), we measure 22 new redshifts not reported in their analysis, and miss 34 of their identifications. Most of the sources we disagree on are faint cluster members. We attribute these differences to the different methods used for the extraction of spectra.

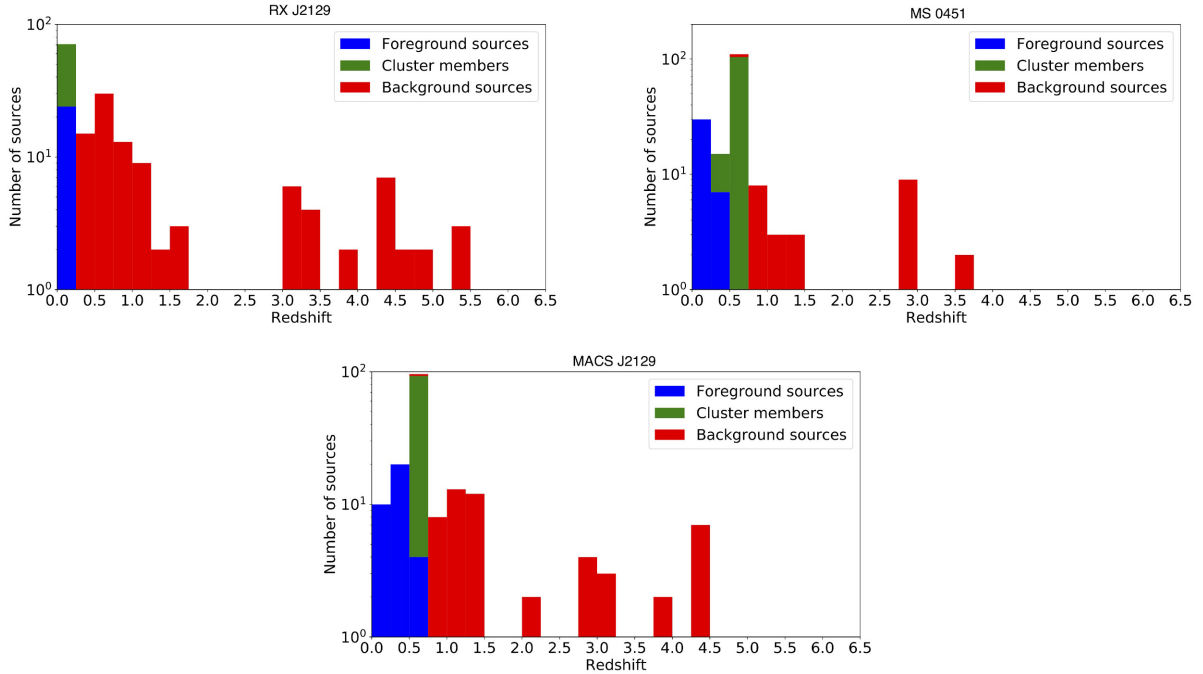**Figure 1.** Redshift distribution of the sources with QF $\geq$ 2 extracted within the MUSE datacubes for RX J2129, MS 0451, and MACS J2129.

2.4.2 MS 0451

We extracted 171 sources with redshifts ranging from 0.0 to 4.85 from the MUSE datacube. Among them, 112 are identified as cluster members, with $0.5307 < z < 0.5652$, 24 sources are identified as foreground objects, 35 are identified as background sources.

2.4.3 MACS J2129

We extracted 189 sources with redshifts ranging from 0.0 to 4.92. Among them, 89 are identified as cluster members with $0.5737 < z < 0.6032$, 39 as foreground objects, and 61 as background sources. The comparison of our measurements with those reported in Caminha et al. (2019) yields similar results to RX J2129, with 16 new redshifts not reported in their analysis, and 25 of their measurements that we miss.

3 STRONG-LENSING ANALYSES

We use the LENSTOOL software (Kneib et al. 1996; Jullo et al. 2007) to perform the strong-lensing analysis of each cluster. We started from existing strong-lensing models, referred to as *fiducial models* in the following, which were either already published, or shared privately with our team. Starting from these *fiducial models*, we use the newly measured redshifts to carry out the identification of new cluster members, and multiple image systems. When possible, we also add the spectroscopic redshift information to already identified multiple image systems, and/or confirm counter-images of the same system.

3.1 Mass modeling method

With LENSTOOL (Jullo et al. 2007), we decompose the cluster gravitational potential into large-scale haloes to model the main dark matter component(s) of the clusters, Φ_{c_i}, and subhaloes to model the

cluster galaxies, Φ_{p_j}, according to

$$\Phi_{tot} = \sum_i \Phi_{c_i} + \sum_j \Phi_{p_j}. \tag{1}$$

Large-scale haloes and subhaloes are described with Pseudo Isothermal Elliptical Mass Distribution profiles (PIEMD; Kassiola & Kovner 1993; Limousin, Kneib & Natarajan 2005; Elíasdóttir et al. 2007), which are parametrized with a core radius, r_c, and a truncation radius, r_t, to calculate the projected mass density:

$$\Sigma(R) = \frac{\sigma^2}{2G} \frac{r_t}{r_t - r_c} \left(\frac{1}{\sqrt{R^2 + r_c^2}} - \frac{1}{\sqrt{R^2 + r_t^2}} \right), \tag{2}$$

where G is the gravitational constant. The projected radius, $R^2 = x^2/(1 + e)^2 + y^2/(1 - e)^2$, is defined with the module of the complex ellipticity, **e** from Natarajan & Kneib (1997), $e = (a^2 - b^2)/(a^2 + b^2)$. In practice, $\mathbf{e} = e \times e^{2i\theta}$, where θ is the orientation angle of the ellipse seen in the cluster from the observer point of view. a and b are, respectively, the semimajor and the semiminor axes of the mass distribution, and σ is the 1D-velocity dispersion. The position of the centre, defined by (x, y), the module of the ellipticity, e, the orientation angle, θ, the truncation and core radii, r_c and r_t, and the velocity dispersion, σ, are the seven parameters needed to describe a PIEMD.

As pointed out by Jullo et al. (2007), the optimization of seven parameters per subhalo would lead to an underconstrained mass model. We thus consider that the luminosity of cluster galaxies is a good tracer of their mass (see the discussion in Harvey, Kneib & Jauzac 2016). Following such assumption, the position and ellipticity of each subhalo are fixed to their luminous counterpart, measured with SEXTRACTOR (Bertin & Arnouts 1996). The total mass of the subhalo is then measured by rescaling the remaining PIEMD parameters for each cluster galaxy, σ, r_c, and r_t, to the ones of a reference galaxy with a luminosity L^*, following the Faber & Jackson

Table 5. List of the multiple images used as constraints in our new LENSTOOL strong-lensing mass model of RX J2129. System 1 was identified by Richard et al. (2010), and its spectroscopic redshift first measured by Belli et al. (2013). Systems 2 was studied in detail in Desprez et al. (2018). Systems 3 and 5 were reported in Zitrin et al. (2015). Systems 6, 7, and 8 are new identification from the MUSE observations. Column 1 is the ID of the image, columns 2 and 3 give the RA and Decl. in degrees (J2000) of each image, column 4 the spectroscopic redshift measured if available, and column 5 the redshift predicted by the best model when no spectroscopic information is available. Spectroscopic redshifts are highlighted in bold when confirmed/measured with MUSE. The rms for each image is given in column 6 in arcseconds. *We here fix the redshift of System 2 to the photometric redshift measured by Desprez et al. (2018).

ID	RA [J2000]	Decl. [J2000]	z_{spec}	z_m	rms (arcsec)
1.1	322.42038	0.08832	1.522	–	0.32
1.2	322.42017	0.08976	1.52	–	0.19
1.3	322.41796	0.09327	1.52	–	0.12
2.1	322.42900	0.10833	*1.61	–	0.07
2.2	322.42856	0.10841	*1.61	–	0.11
2.3	322.42912	0.10807	*1.61	–	0.09
2.4	322.42867	0.10790	*1.61	–	0.09
3.1	322.41843	0.08537	1.52	–	0.35
3.2	322.41767	0.09027	1.52	–	0.34
3.3	322.41572	0.09222	1.52	–	0.10
4.1	322.41373	0.09208	3.427	–	0.11
4.2	322.41443	0.08863	3.427	–	0.38
4.3	322.41754	0.08386	3.427	–	0.42
5.1	322.41659	0.08774	0.916	–	0.27
5.2	322.41627	0.08810	0.916	–	0.17
5.3	322.41463	0.09236	0.916	–	0.12
6.1	322.41492	0.09038	0.679	–	0.26
6.2	322.41663	0.08674	0.679	–	0.27
6.3	322.41516	0.08898	0.679	–	0.69
7.1	322.41675	0.08779	3.08	–	0.02
7.2	322.41700	0.08739	3.08	–	0.27
7.3	322.41376	0.09420	3.08	–	0.69
8.1	322.41592	0.09150	1.52	–	0.31
8.2	322.41694	0.09031	1.52	–	0.44
8.3	322.41854	0.08492	1.52	–	0.25

(1976) relation:

$$\begin{cases} \sigma = \sigma^* \left(\frac{L}{L^*} \right)^{1/4} \\ r_c = r_c^* \left(\frac{L}{L^*} \right)^{1/2} \\ r_t = r_t^* \left(\frac{L}{L^*} \right)^{1/2} \end{cases}, \tag{3}$$

from which the total mass of each subhalo is derived following:

$$M = \frac{\pi}{G} (\sigma^*)^2 r_c^* \left(\frac{L}{L^*} \right), \tag{4}$$

where σ^*, r_t^*, and r_c^*, are the reference velocity dispersion, truncation, and core radii, respectively. It was shown in previous models that r_c^* is small in galaxy-scale haloes and thus plays a minor role in the mass models (e.g. Covone et al. 2006; Limousin et al. 2007; Elíasdóttir et al. 2007). We thus adopt a conservative value of $r_c^* \sim 0.15$ kpc for all three clusters.

For each model, we start by optimizing one large-scale halo per cluster. The brightest cluster galaxy (BCG), and cluster members located in the vicinity of multiple images are individually optimized as they act as small-scale perturbers. We then add a second large-scale potential in the optimization process when a set of multiple images concentrated in a given region of the cluster core cannot be reproduced with a simple one-halo mass model.

Table 6. List of the multiple images used as constraints in our new LENSTOOL strong-lensing mass model of MS 0451. Systems A, B, and C were reported by Borys et al. (2004). Systems E, F, G and I were identified by MacKenzie et al. (2014). Systems D, H, and J to P were detected by our team, and will be presented in an upcoming analysis (Richard et al. in preparation). Systems R and S are new detections from this analysis. The table elements are the same as Table 5. *System P was flagged as insecured, and thus not used in the model.

ID	RA [J2000]	Decl. [J2000]	z_{spec}	z_{model}	rms (arcsec)
A.1	73.55396	−3.01482	2.91	–	0.23
A.2	73.55389	−3.01595	2.91	–	0.18
A.3	73.54630	−3.02404	2.91	–	0.20
B.1	73.55335	−3.01232	–	2.9 ± 0.3	0.13
B.2	73.55285	−3.01707	–	2.9 ± 0.3	0.41
B.3	73.54553	−3.02348	–	2.9 ± 0.3	0.31
C.1	73.55339	−3.01325	–	2.8 ± 0.2	0.14
C.2	73.55304	−3.01656	–	2.8 ± 0.2	0.17
C.3	73.54545	−3.02380	–	2.8 ± 0.2	0.26
D.1	73.55409	−3.01469	–	2.9 ± 0.1	0.37
D.2	73.55399	−3.01640	–	2.9 ± 0.1	0.06
D.3	73.54658	−3.02401	–	2.9 ± 0.1	0.17
E.1	73.55481	−3.01065	–	2.8 ± 0.2	0.24
E.2	73.55241	−3.01996	–	2.8 ± 0.2	0.23
E.3	73.54911	−3.02226	–	2.8 ± 0.2	0.20
F.1	73.55435	−3.01088	–	2.9 ± 0.3	0.35
F.2	73.55282	−3.01918	–	2.9 ± 0.3	0.59
F.3	73.54775	−3.02268	–	2.9 ± 0.3	0.39
G.1	73.55593	−3.01193	2.93	–	0.41
G.2	73.55271	−3.02124	2.93	–	0.85
G.3	73.55071	−3.02261	2.93	–	0.02
H.1	73.53855	−3.00589	6.7	–	0.10
H.2	73.53687	−3.00773	6.7	–	0.10
H.3	73.53662	−3.00807	6.7	–	0.18
H.4	73.53647	−3.00830	6.7	–	0.22
I.1	73.55342	−3.01089	–	3.1 ± 0.3	1.17
I.2	73.55233	−3.01807	–	3.1 ± 0.3	1.16
I.3	73.54597	−3.02285	–	3.1 ± 0.3	0.55
J.1	73.54901	−3.01848	–	1.7 ± 0.2	0.03
J.2	73.54830	−3.01930	–	1.7 ± 0.2	0.04
K.1	73.55685	−3.01410	–	3.1 ± 0.2	0.76
K.2	73.55352	−3.02183	–	3.1 ± 0.2	0.77
K.3	73.55250	−3.02276	–	3.1 ± 0.2	0.24
L.1	73.54119	−3.01469	–	7.3 ± 0.8	0.53
L.2	73.54191	−3.02009	–	7.3 ± 0.8	0.29
L.3	73.55136	−3.00437	–	7.3 ± 0.8	0.44
M.1	73.54787	−3.01719	–	1.02 ± 0.07	0.38
M.2	73.54822	−3.01656	–	1.02 ± 0.07	0.21
M.3	73.54936	−3.01404	–	1.02 ± 0.07	0.39
O.1	73.54268	−3.01943	–	1.8 ± 0.1	0.54
O.2	73.54370	−3.01400	–	1.8 ± 0.1	1.12
O.3	73.54807	−3.00859	–	1.8 ± 0.1	1.63
*P.1	73.54574	−3.01966	–	–	–
*P.2	73.54872	−3.01730	–	–	–
R.1	73.53630	−3.01234	3.765	–	0.59
R.2	73.53618	−3.01331	3.765	–	0.23
R.3	73.54229	−3.00485	3.765	–	0.61
S.1	73.54723	−3.01284	4.451	–	1.39
S.2	73.54627	−3.01263	4.451	–	1.22

Table 7. List of the multiple images used as constraints in our new LENSTOOL strong-lensing mass model of MACS J2129. Systems 1–9 have been identified by Monna et al. (2017). Systems 10 is newly identified in this work. Systems 11–14 were initially identified by Caminha et al. (2019). Table elements are the same as in Table 5.* These images are not included in our model as their spectroscopic redshift is not considered secure. System 14 corresponds to System 5 in Caminha et al. (2019).

ID	R A [J2000]	Decl. [J2000]	z_{spec}	z_{model}	rms (arcsec)
1.1	322.35797	−7.68588	1.36	−	0.35
1.2	322.35965	−7.69082	1.36	−	0.10
1.3	322.35925	−7.69095	1.36	−	0.24
1.4	322.35712	−7.69109	1.36	−	0.31
1.5	322.35764	−7.69115	1.36	−	0.11
1.6	322.35861	−7.69489	1.36	−	0.60
2.1	322.35483	−7.6907	1.048	−	0.736
2.2	322.35477	−7.6916	1.048	−	0.08
2.3	322.35538	−7.69332	1.048	−	0.53
3.1	322.35022	−7.68886	2.24	−	0.18
3.2	322.35011	−7.68950	2.24	−	0.76
3.3	322.35095	−7.69577	2.24	−	0.40
4.1	322.36642	−7.68674	2.24	−	0.29
4.2	322.36693	−7.68831	2.24	−	0.35
4.3	322.36679	−7.69497	2.24	−	0.41
5.1	322.36422	−7.69387	−	1.67 ± 0.03	0.16
5.2	322.36460	−7.69137	−	1.67 ± 0.03	0.57
5.3	322.36243	−7.68493	−	1.67 ± 0.03	0.27
6.1	322.35094	−7.69333	6.85	−	0.69
6.2	322.35324	−7.69744	6.85	−	0.87
6.3	322.35394	−7.68164	6.85	−	1.04
7.1	322.35714	−7.69425	1.357	−	0.62
7.2	322.35625	−7.69172	1.357	−	0.84
7.3	322.35670	−7.68554	1.357	−	0.52
8.1	322.35698	−7.68924	4.41	−	0.54
8.2	322.36167	−7.68808	4.41	−	1.61
8.3	322.35860	−7.68491	4.41	−	1.86
8.4	322.36035	−7.70094	4.41	−	1.01
8.5	322.35419	−7.68876	4.41	−	1.27
9.1	322.36651	−7.68689	2.24	−	0.69
9.2	322.36695	−7.68820	2.24	−	0.43
9.3	322.36666	−7.69525	2.24	−	0.79
10.1	322.35762	−7.68471	4.41	−	0.23
10.2	322.35499	−7.68896	4.41	−	1.39
11.1	322.36334	−7.69707	3.108	−	0.79
11.2	322.36491	−7.69010	3.108	−	0.48
11.3	322.36167	−7.68362	3.108	−	0.88
12.1	322.35455	−7.68518	3.897	−	0.22
12.2	322.35278	−7.68841	3.897	−	0.45
*12.3	322.35736	−7.69977	3.897	−	−
13.1	322.35330	−7.69113	1.359	−	0.45
13.2	322.35391	−7.68758	1.359	−	0.45
13.3	322.35443	−7.69441	1.359	−	0.13
*14.1	322.36131	−7.68590	1.452	−	−
*14.2	322.36248	−7.69142	1.452	−	−
*14.3	322.36259	−7.69360	1.452	−	−

LENSTOOL uses a Markov Chain Monte Carlo (MCMC) process to sample the posterior density of the model, expressed as a function of the likelihood of the model, defined in Jullo et al. (2007). In practice, we minimize

$$\chi^2 = \sum_i \chi_i^2 \,, \tag{5}$$

where

$$\chi_i^2 = \sum_{j=1}^{n_i} \frac{(\theta_{obs}^j - \theta^j(\boldsymbol{p}))^2}{\sigma_{ij}^2} \,. \tag{6}$$

θ_{obs}^j is the vector position of the observed multiple image j, θ^j is the predicted vector position of image j, n_i is the number of images in System i, and σ_{ij} is the error on the position of image j (fixed at $\sim$ 0.5 arcsec for multiple images to account for both errors on image positions between MUSE and *HST* images and line of sight effects as described in Jullo et al. 2007, 2010a). As a consequence, the most likely model minimizes the distance between the observed positions of the multiple images and their predicted position by the model, the rms.

In what follows, we describe the set of multiple image systems used to constrain the new mass models for each cluster, and then detail the selection of independently optimized haloes.

3.2 Multiple images

We use the catalogues of sources described in Section 2.4 to carry out the search for multiple images. We start by comparing our data to the lists of multiple images used in the *fiducial models*, and thus add the spectroscopic redshift information when available. For each sources identified as background in our catalogues, and not already identified by previous strong-lensing analyses, we use the *fiducial models* to predict their multiplicity.

If a background source is confirmed as multiple, the narrow-band datacube at the wavelength corresponding to its maximum emission is used, and combined with composite colour images made from different combinations of *HST* filters, to identify all the multiple images of the system. When a multiple image system is then confirmed, it is added as a constraint to the new mass model. The lists of multiple image systems used in RX J2129, MS 0451, and MACS J2129 are given in Tables 5–7, respectively. They are also highlighted with white circles in Figs 2–4, respectively. Further details about the redshift measurements of multiple image systems are presented in Appendix B for MS 0451 (e.g. the strongest spectral lines, together with *HST* stamps of the multiple images), and we refer the reader to Caminha et al. (2019) for similar information regarding RX J2129 and MACS J2129.

3.2.1 RX J2129

Our *fiducial model* was built from the parametric model presented in Zitrin et al. (2015), which includes four multiple images, and adapted within the LENSTOOL framework. We here present the results out of our redshift extractions from the MUSE datacube, and compare them with the results presented in Caminha et al. (2019) who analysed the same MUSE observations.

Our spectroscopic redshift measurements for System 1 ($z = 1.522$, QF = 3, Mg/Fe absorber), System 5 ($z = 0.916$, QF=2, O II emitter), and System 3 ($z = 1.52$, QF = 3, Mg absorber) are in excellent agreement with the previous measurements presented by Caminha et al. (2019). One will note that the redshift of System 1 was initially measured by Belli et al. (2013). Moreover, we confirm the initial identification of 4 new multiple image Systems reported in Caminha et al. (2019). System 4 ($z = 3.4270$, QF=3, [O II] emitter), System 6 ($z = 0.6786$, QF = 3, [O II] emitter), System 7 ($z = 3.08$, QF = 3, Ly α emitter), and System 8 ($z = 1.52$, QF = 3, Mg and Fe absorbers) are confirmed triply imaged systems.

The main difference between the constraints used by Caminha et al. (2019) and our analysis is the inclusion of System 2 here, a
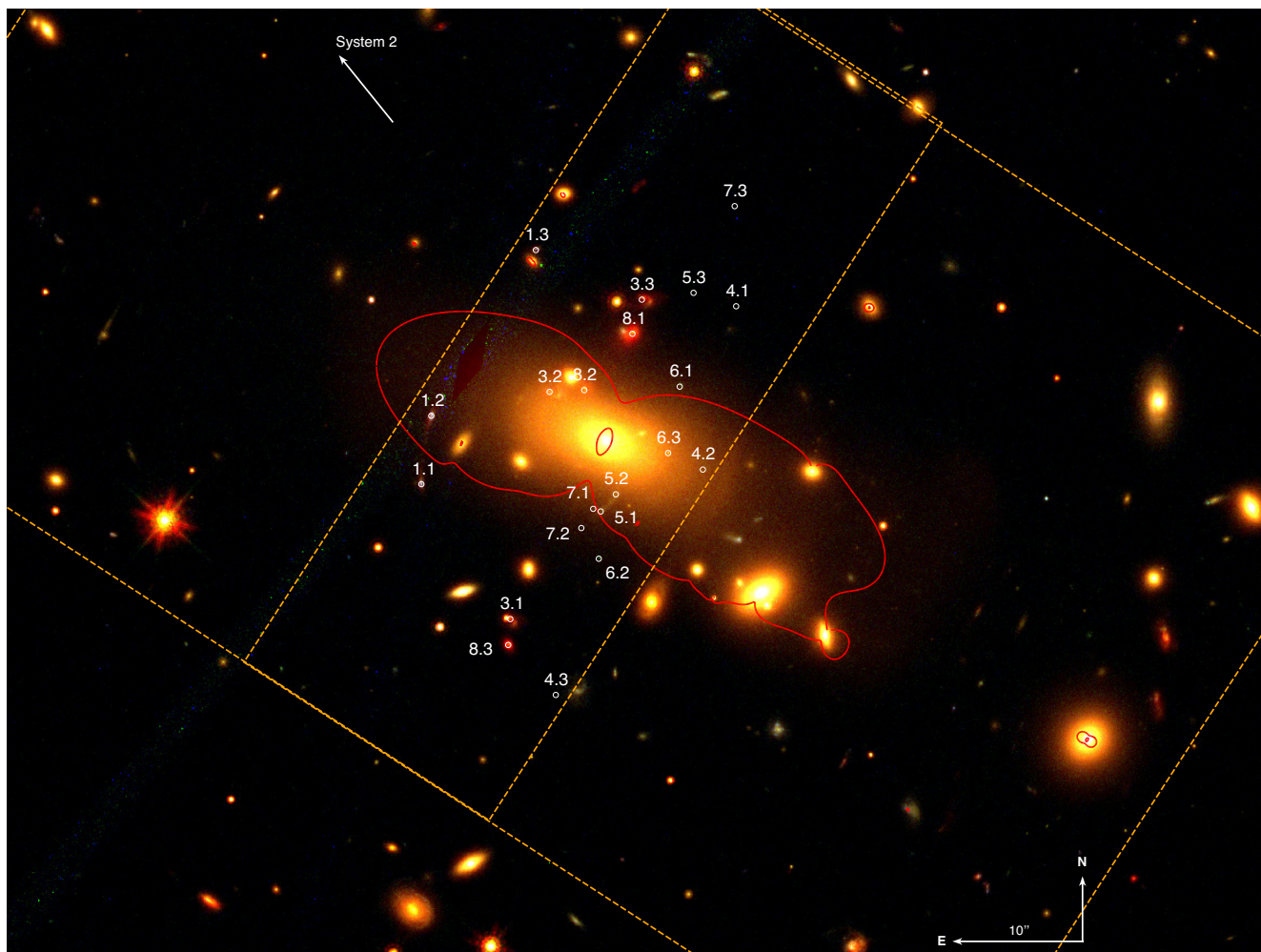
Figure 2. *HST* composite colour image of System 2 in RX J2129 using F475W, F606W, and F814W pass-bands. Multiple images used as constraints are highlighted by white circles.

galaxy–galaxy lensing system. It is located relatively far from the cluster center, 81 arcsec from the BCG, in the vicinity of a massive isolated galaxy outside the field of view covered by MUSE (i.e. R A = 322.429, Decl. = 0.1082), and can be seen in Fig. 5. Desprez et al. (2018) studied this System in detail, and its impact on the overall mass reconstruction of the cluster. For the analysis presented here, we assume the photometric redshift measured by Desprez et al. (2018), $z = 1.61$.

3.2.2 MS 0451

Our *fiducial model* is based on the LENSTOOL model from MacKenzie et al. (2014), then revised by the identification of 8 new multiple image systems, including a $z = 6.7$ quintuple image in the north of the cluster (Knudsen et al. 2016, and will be presented in detail in Richard et al. in preparation). We now present the new measurements for MS 0451, and thus the constraints added to our new mass model.

3.2.2.1 New multiple image systems
We report the identification of two new systems of multiple images at high redshifts. System R ($z = 3.7645$, QF = 3) is composed of three multiple images, and is located in the poorly constrained northern region of the cluster. System S ($z = 4.4514$, QF = 3) is predicted to be quadruply imaged but only

two multiple images could be identified. These sources are Ly α emitters identified thanks to the blind-search carried out directly in the datacube with MUSELET. These two systems are located within two poorly constrained regions of the cluster, and are playing a substantial role in the improvement of the accuracy of the model as described in Section 4. The strongest MUSE spectral lines of Systems R and S are presented in Fig. B1.

3.2.2.2 Confirmation and measurement of known systems
We report the measurement of a spectroscopic redshift for all three multiple images of System G, $z = 2.93$ (QF=3, Ly α emitter). We also measure a spectroscopic redshift for System A, $z = 2.92$, which is in agreement with the previous measurement from Borys et al. (2004) and Berciano Alba et al. (2010). The strongest MUSE spectral lines of System G are presented in Fig. B2.

3.2.2.3 Other systems
The redshift of System H is measured at $z = 6.7$ by Knudsen et al. (2016) and Richard et al. (in preparation). Image P.2 is located in a bright region surrounding the BCG which makes it difficult to identify. Moreover Image P.1 is located in the vicinity of a cluster member which increases the uncertainty on the location of the system. Therefore, System P was flagged as insecure and is not used
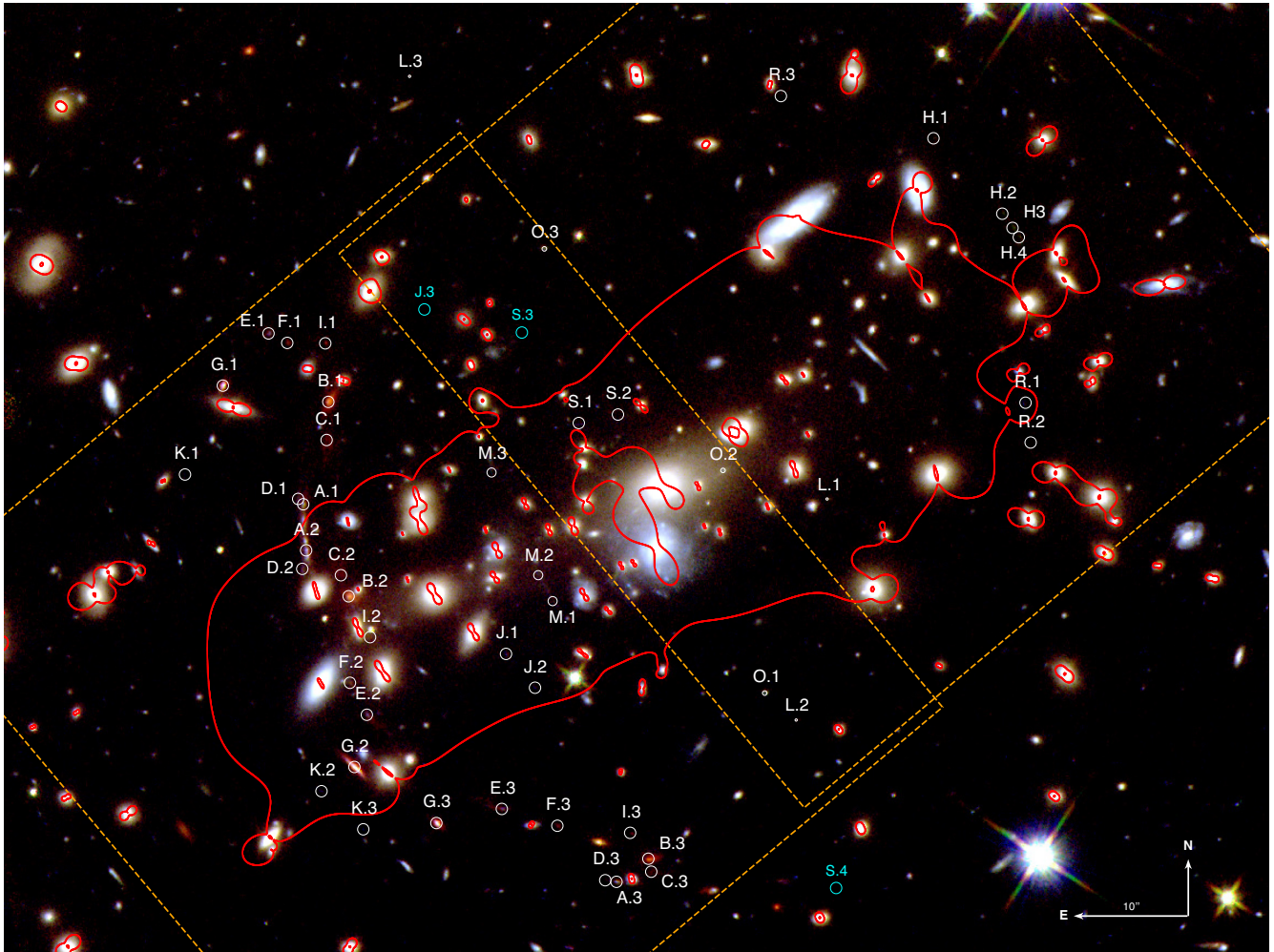
Figure 3. *HST* composite colour image of RX J2129 using F475W, F814W, and F160W pass-bands. Multiple images used as constraints are highlighted by white circles. Critical lines are displayed for a source at redshift $z = 1.52$ in red. Orange dashed squares show the MUSE fields of view. System 2 is outside the field of view, and can be seen in Fig 5.

in the model. For the remaining 11 systems without spectroscopic confirmation, their redshift is being optimized by the model.

3.2.3 MACS J2129

Our *fiducial model* was built from the model presented in Monna et al. (2017) combining CLASH photometry (see Table 2) and VLT/VIMOS spectroscopy (PI: Rosati, ID: 186.A-0798). It relies on 9 multiple image systems, 7 of which were spectroscopically confirmed back then. We then extracted spectroscopic redshifts from the MUSE datacubes, and compared our results with Caminha et al. (2019) who analysed the same MUSE observations.

Our analysis measures similar redshifts to Caminha et al. (2019) for Systems 1, 2, 3, 7, and 8, in good agreement with Monna et al. (2017) measurements. We measure a redshift of $z = 4.41$ (QF = 3, Ly α emitter) for Images 8.1, 8.2, and 8.3, in agreement with the redshift of 8.1 measured by Monna et al. (2017), and confirmed by Caminha et al. (2019). The fourth image of System 8, Image 8.4, is outside the MUSE field of view. Caminha et al. (2019) identified the counter-image 8.5 which we confirm as well. We show in Fig. 6 composite colour *HST* stamps of the five images, narrow-band images, and their spectra extracted from the MUSE datacubes. We

cannot obtain reliable redshift measurements from the extracted spectra of Systems 4, 5, and 9. We thus use the spectroscopic redshifts measured with VIMOS in Monna et al. (2017) for Systems 4 and 9 (QF=2), and optimize the redshift of System 5 in our mass model. The redshift of System 6 ($z = 6.85$) was spectroscopically confirmed by Huang et al. (2016), and could not be measured with MUSE since the wavelength corresponding to the maximum emission is greater than the upper limit of the MUSE wavelength range ($\sim$9350 Å), as in the case of the $z = 6.7$ quintuply imaged system in MS 0451 (Knudsen et al. 2016; Richard et al. in preparation).

With this work, we confirm the four new spectroscopic identifications of multiple image systems identified by Caminha et al. (2019), and present the new identification of one system: Systems 10 ($z = 4.41$, QF=3, Ly α emitter), 11 ($z = 3.1081$, QF = 3, Ly α emitter), 12 ($z = 3.897$, QF = 3, Ly α emitter), 13 ($z = 1.3585$, QF=2, [O II] emitter), and 14 ($z = 1.4519$, QF=1, [O II] emitter). System 10 is not identified by Caminha et al. (2019), however they detect Image 10.1 which is listed in the public release of their catalogue.[7] Our model predicts it as quadruply imaged, although only two multiple images could be confirmed with MUSE. This system seems to be linked to

---

[7]http://cdsarc.u-strasbg.fr/viz-bin/Cat?J/A+A/632/A36
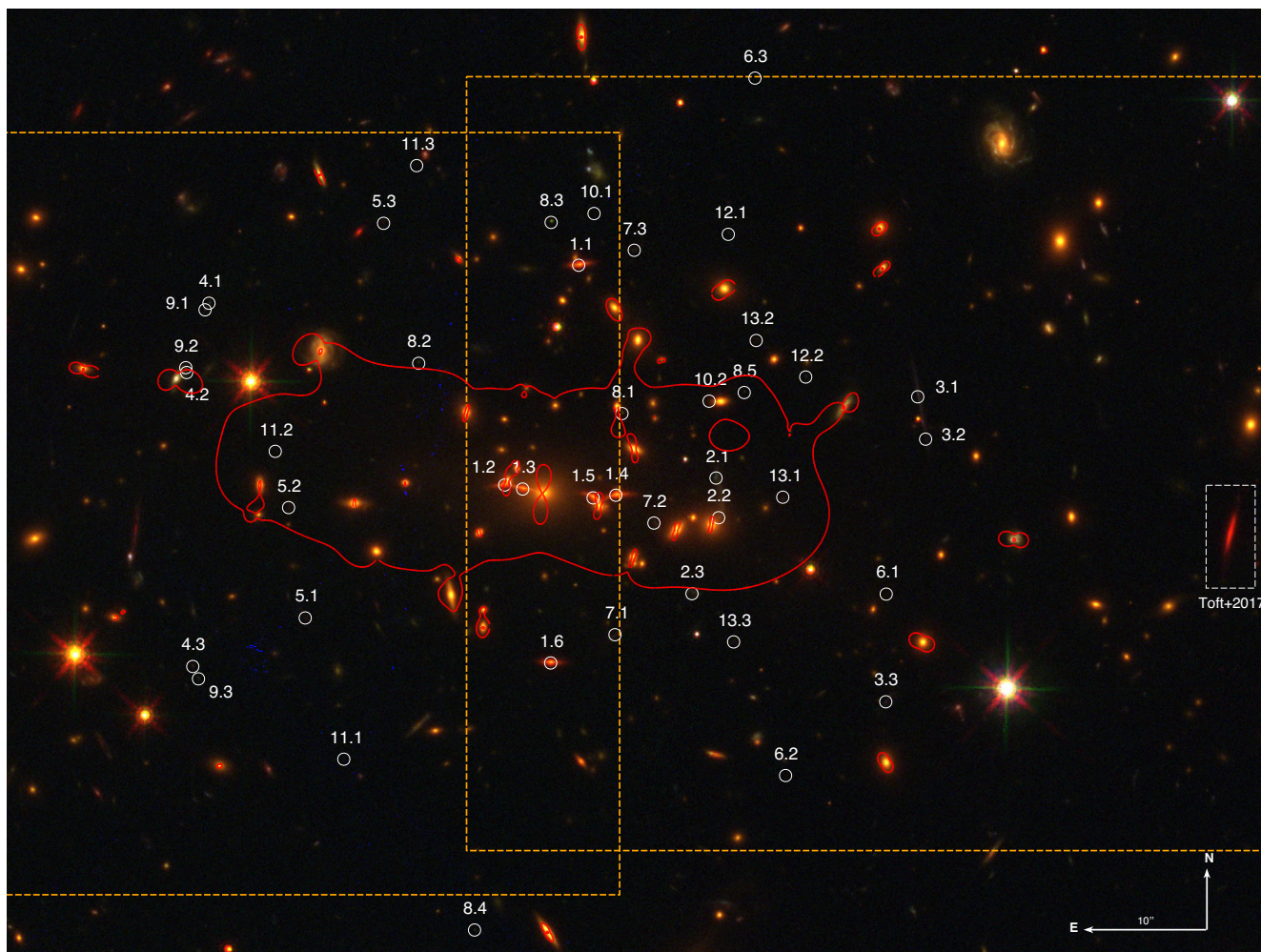
Figure 4. *HST* composite colour image of MS 0451 using F814W, F110W, and F160W pass-bands. Multiple images used as constraints are highlighted by white circles. Cyan circles highlight the predicted positions of the counter-images of System J and System S. Critical lines for a source at redshift $z = 2.9$ (redshift of System A) are shown as red lines. Orange dashed squares show the MUSE fields of view.

System 8, composed of 5 multiple images. Image 10.1 appears to be located close to the Ly α emission of image 8.3, although the two emission regions are well separated. This could imply that the two systems highlight two physically connected lensed galaxies at $z =$ 4.41, System 8 being more UV bright and detected in the *HST* images. Image 10.2 is located relatively close to Image 8.5, separated by a cluster galaxy (G3 in our model discussed in Section 3.3 and visible in Fig. 7); however, the feature is similar to what is visible in the case of Images 8.3/10.1. We find a possible candidate for another image of system 10 located close to Image 8.2, as a faint Ly α tail. However, the detection has a low signal-to-noise ratio, we therefore do not include that image in our model. System 10 is extremely faint in the *HST* image, it is thus difficult to securely identify its fourth counter-image which is predicted outside the MUSE field of view, relatively close to Image 8.4. Fig. 6 shows composite *HST* stamps of Images 10.1 and 10.2, their narrow-band images, and the spectra extracted from the MUSE datacubes, along with the five multiple images of System 8. We therefore include the five images for System 8 in our model, and the two images of System 10 detected in the MUSE datacubes. Regarding System 14 (System 5 in Caminha et al. 2019), our spectroscopic measurement is flagged as unsecure, we therefore decide to not include this system as a constraint in our strong-lensing

mass model, but list it in Table 7 for consistency with Caminha et al. (2019). Caminha et al. (2019) also lists a counter-image for System 12, Image 12.3 in Table 7, System 9 and Image 9c in their analysis. This counter-image is not spectroscopically confirmed, and we are not convinced by its colour and morphology in the *HST* imaging. We thus only consider it as a candidate.

3.3 Cluster- and galaxy-scale components

For each cluster, we compare the MUSE spectroscopically confirmed cluster members to the list of cluster galaxies used in the *fiducial models*. MUSE observations allowed us to identify 43, 112, and 89 cluster galaxies for RX J2129, MS 0451, and MACS J2129, respectively. Among those, 15 in RX J2129 and 4 in MACS J2129 are new detections, i.e. not reported by Caminha et al. (2019). We combine those with the cluster member galaxies identified by previous works, using standard colour-magnitude red-sequence selections as well as spectroscopic identifications with different instruments. We use cluster identifications from Desprez et al. (2018), Monna et al. (2017), and Richard et al. (in preparation) for RX J2129, MS 0451, and MACS J2129, respectively. In total, we used 70, 144, and 151 cluster members for the modelling of RX J2129, MS 0451,
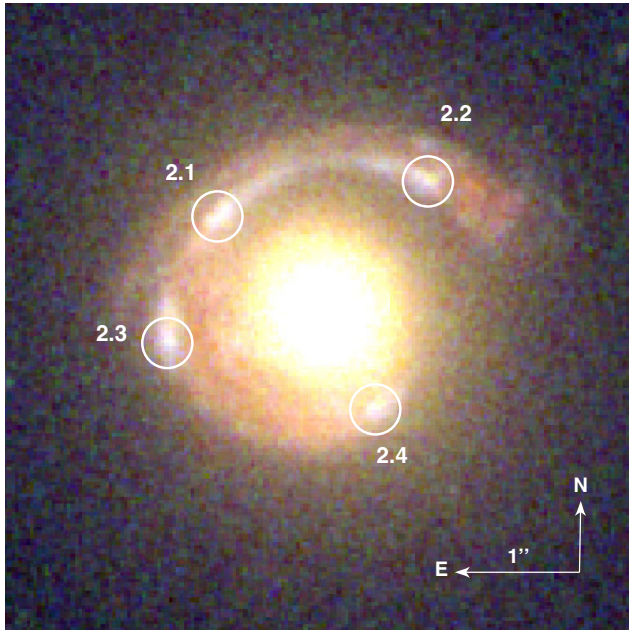
Figure 5. *HST* composite colour image of MACS J2129 using F475W, F814W, and F160W pass-bands. Multiple images used as constraints are highlighted by white circles. Critical lines are displayed as red lines for a source at redshift $z = 1.36$. Orange dashed squares show the MUSE fields of view. The white dashed box highlight the galaxy at $z = 2.1478$ detected by Toft et al. (2017).

and MACS J2129, respectively. We used the method presented in Section 2.4 to optimize the parameters of each subhalo. As explained before, we optimize a selection of large-scale and galaxy-scale haloes for each cluster. The best-fitting parameters obtained are listed in Table 8, and discussed in this section. For scaling relations, the reference magnitudes are mag$_{F814W}$ = 17.49, mag$_{F814W}$ = 18.69, and mag$_{F814W}$ = 19.19 for RX J2129, MS 0451, and MACS J2129, respectively. The shapes of the individually optimized potentials from the best fit are shown in the right-hand panel of Fig. 7.

3.3.1 RX J2129

Our model contains one large-scale halo described by a PIEMD mass component. We model individually the BCG and include an isolated cluster galaxy (G1 in Table 8), which acts as the lens for System 2 as detailed in Desprez et al. (2018). The four multiple images of System 2 are attributed to galaxy–galaxy lensing and are used as constraints in our model as shown in Table 5. One can see a zoom in on this lensing configuration in Fig. 2.

Our best-fitting mass model has an rms = 0.29 arcsec. The best-fitting parameters of the model are given in Table 8, and the center of the cluster is chosen as (R A = 322.41651, Decl. = 0.08923). In order to check the impact of the addition of free parameters by the inclusion of G1 as an individual potential, we run a model which treats G1 as a standard cluster member, i.e. following the Faber & Jackson (1976) relation. While the rms (χ^2, *dof*) of this model is not significantly different from our best-fitting mass model, 0.28 arcsec (8, 22) versus 0.29 arcsec (9, 24), it has a local impact. Indeed, the rms of System 2 is 0.15 arcsec, while we obtain an rms of 0.09 arcsec when G1 is included. We therefore conclude that G1 improves the model and is necessary to precisely recover the geometry of System 2.

3.3.2 MS 0451

Our initial model only included one large-scale halo centred on the BCG of MS 0451. However, such model could not reproduce precisely the multiple images located in the north of the cluster, with an rms $> 1.0''$ for all systems. With a single cluster-scale halo model, the critical line at redshift $z = 6.7$, corresponding to the redshift of System H, would not pass between Images H.2 and H.3, nor Images H.3 and H.4. The same applies for System R which, in this context, has an rms > 1 arcsec. We thus looked at the distribution of cluster members, and identified two groups of galaxies, at the cluster redshift, located north of the cluster BCG. We thus run a new model that included a second large-scale halo, also modelled with a PIEMD, centred between these two groups. We note that we also run a model including three large-scale haloes (one for the cluster and the other two for the galaxy groups); however, the best-fitting model was not statistically better than the 2-halo one. We therefore decided to consider the simplest of the two models.

The BCG was modeled separately using a PIEMD profile where σ and r_{cut} are being optimized independently. We also include four independent subhaloes to model galaxies located in the foreground of the cluster ($z = 0.0623$ – IDs G1, G2, G3, and G4 in Table 8). As the multiplane optimization is not yet finalized in LENSTOOL, the impact of a given foreground galaxy is being assessed by projecting its mass component in the cluster plane.

Moreover, the blind search in the MUSELET narrow-band datacube revealed an unidentified cluster member ($z = 0.531$) located in the vicinity of Image R.1, and too faint to be seen in the *HST* images. We thus chose to include this cluster member as an individually optimized potential in our mass model as it acts as a local small-scale perturber for System R (potential G5 in Table 8, O II emitter, QF = 3). Finally, we add one more galaxy-scale halo, the cluster member identified as G6, located closely to Image K.1.

Our best-fitting mass model has an rms = 0.60 arcsec. The best-fitting parameters of the model are given in Table 8, and the centre of the cluster is chosen as (R A = 73.54520, Decl. = −3.01439). This mass model is used for the combined strong and weak-lensing analysis of MS 0451 presented in Tam et al. (2020).

As was done for RX J2129, a model was run excluding all individual galaxy-scale haloes, G1, G2, G3, G4, G5, and G6. The resulting model has an rms (χ^2, *dof*) of 1.59 arcsec (478,34), more than a factor of 2 from our best-fitting model which has an rms (χ^2, *dof*) of 0.6 arcsec (68, 18), demonstrating the need for these galaxies to be modelled individually. We also assess specifically the impact of including galaxies G1, G2, G3, and G4 that are known to be foreground objects as mentioned before. We thus run a model that excludes these four galaxy-scale haloes. The resulting best-fitting model has an rms (χ^2, *dof*) of 0.92 arcsec (159, 26). This again shows the necessity to include those as individual potentials, ignoring their results in a degradation of the goodness of the fit. To go even further, with this one model the rms of System H, the quadruply imaged galaxy at $z = 6.7$, is degraded to 0.5 arcsec, to be compared with 0.16 arcsec with our best-fitting mass model, and the model cannot reproduce properly the lensing configuration. We then assess the impact of G6 in our mass model. We run a model which excludes this one individual galaxy-scale halo. The resulting model gives an rms of 0.59 arcsec. Compared to our best-fitting model presented before which has an rms of 0.6 arcsec, the improvement is not significant. However, the presence of G6 impacts the rms of several systems, with the most significant one being System H with an rms degraded to 0.48 arcsec. This system being a stringent constraints to our model, we also consider G6 as necessary to our model.
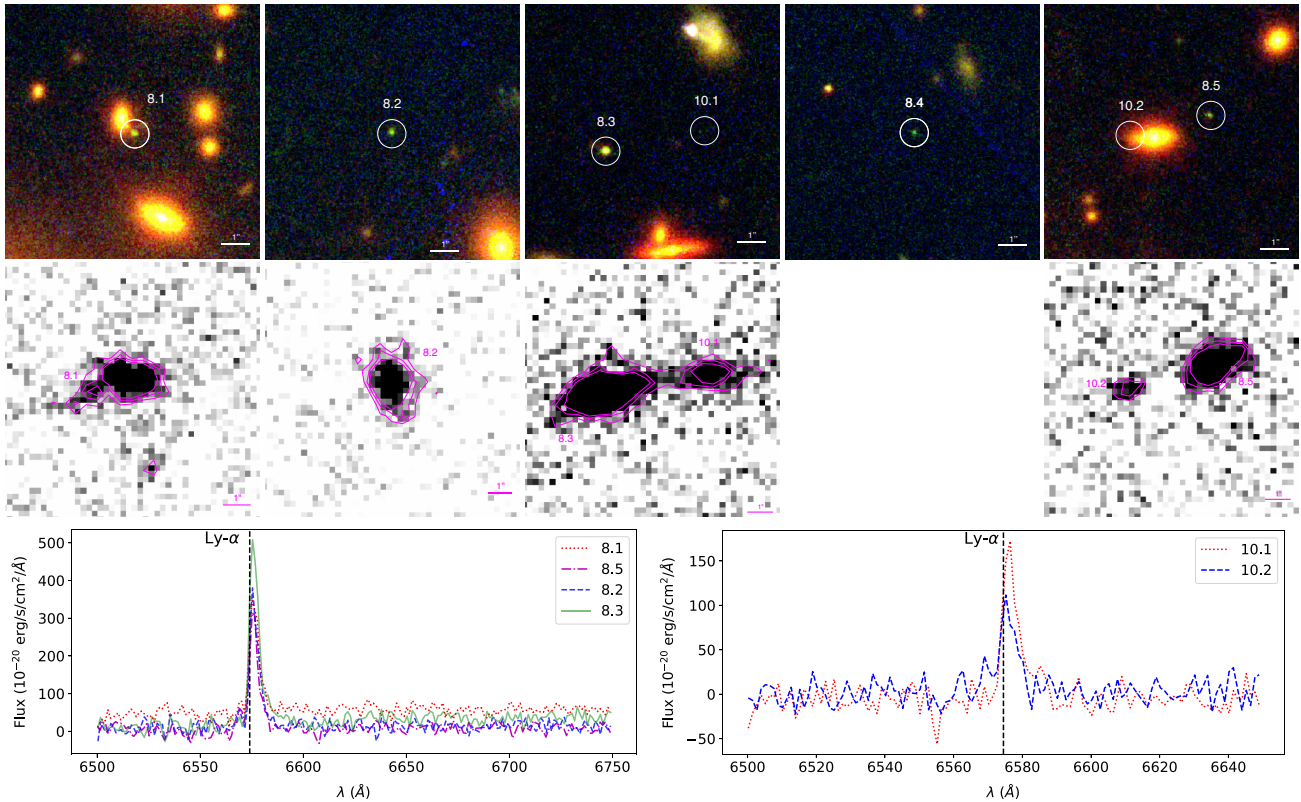
Figure 6. MACS J2129 – System 8 (System 10 in Caminha et al. 2019) and System 10 with a measured spectroscopic redshift, $z = 4.41$. *Top:* Composite colour *HST* stamps of the multiple images 8.1 to 8.5, including 10.1 and 10.2 close to 8.3 and 8.5. *Middle:* MUSELET narrow-band datacube stamps at the wavelength of the maximum emission of the source, i.e. $\lambda = 6577\mathring{A}$ (right-hand panel). The contours are displayed in magenta for 2, 3, and $4 \times 10^{-20} \, \mathrm{erg \, s^{-1} \, arcsec^{-2}}$. *Bottom:* Extracted spectra from the MUSE datacube centred on the most prominent lines for images of System 8 (left) and System 10 (right).

3.3.3 MACS J2129

We use a similar approach to MS 0451 by starting with a model as simple as possible, and, thus, including only one large-scale halo. However, the two most Easterly systems, Systems 3 and 6, were poorly reproduced with this model, with an rms greater than 1 arcsec. We thus decided to add a second large-scale halo centred on a galaxy group located north-east of the BCG. All large-scale haloes are modelled using PIEMDs, and all their parameters are being optimized except for the truncation radius which is set to 1000 kpc.

We individually optimize the BCG of the cluster. We then add two galaxy-scale haloes to model galaxies identified as small-scale perturbers by Monna et al. (2017), due to their proximity to the sextuply imaged System 1 (G1 and G2 in Table 8). Moreover, Images 10.2 and 8.1 are both located near cluster galaxies, encouraging us to include those as individual potentials in our mass model (G3 and G4 in Table 8).

Our best-fitting mass model has an rms = 0.74 arcsec. The best-fitting parameters of the model are given in Table 8, and the centre of the cluster is chosen as (R A = 322.35878, Decl. = −7.69100). As for RX J2129 and MS 0451, we test the necessity of the individual galaxy-scale potentials in our best model. When excluding all individual galaxy-scale haloes, we obtain an rms (χ^2, *dof*) of 1.05 arcsec (184, 41), to be compared to 0.74 arcsec (90, 31) with our best-fitting model. Such a difference comforts us in our choice of modelling G1, G2, G3, and G4 individually due to their proximity to some of the multiple images in the cluster.

4 RESULTS AND DISCUSSIONS

As presented in Section 3, the optimization of RX J2129, MS 0451, and MACS J2129 mass models were done using LENSTOOL (Jullo et al. 2007), and the best-fitting parameters for each model are given in Table 8. The list of multiple images used as constraints, together with their spectroscopic redshift or the optimized one from the models when included as a free parameter, and the rms obtained for each multiple image are provided in Tables 5–7. In this section, we discuss the improvements on the mass models brought by the MUSE data for each cluster, considering their mass distributions, density profiles, rms, and compare our results with previously published works.

4.1 RX J2129

Our best mass model is constrained by 8 multiple image systems, 7 of them spectroscopically confirmed, and is composed of 71 potentials including one large-scale halo and 2 galaxy-scale haloes independently optimized. The best-fitting model has an rms of 0.29 arcsec. The left-hand panel of Fig. 8 shows the density profiles for both the *fiducial* and our best models. One can see that the new model predicts a significantly higher density in the very inner core of RX J2129, $R > 10$ kpc, compare to the *fiducial model*, which then takes over at larger radii. In terms of total mass within the multiple image region, $R < 70$ kpc, we measure $M(\mathrm{R} < 70 \, \mathrm{kpc}) = (0.30 \pm 0.01) \times 10^{14} \, \mathrm{M_\odot}$, in perfect agreement with $M_{\mathrm{fiducial}}(\mathrm{R} < 70 \, \mathrm{kpc}) = (0.30 \pm 0.01) \times 10^{14} \, \mathrm{M_\odot}$.
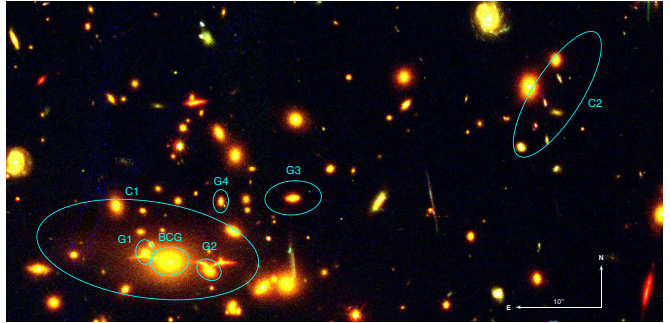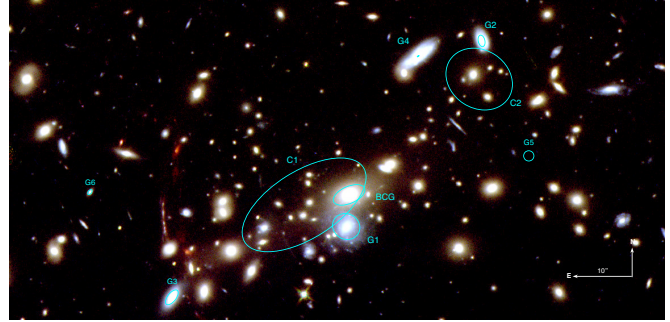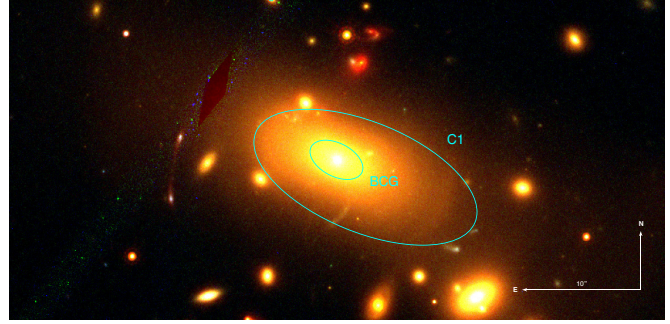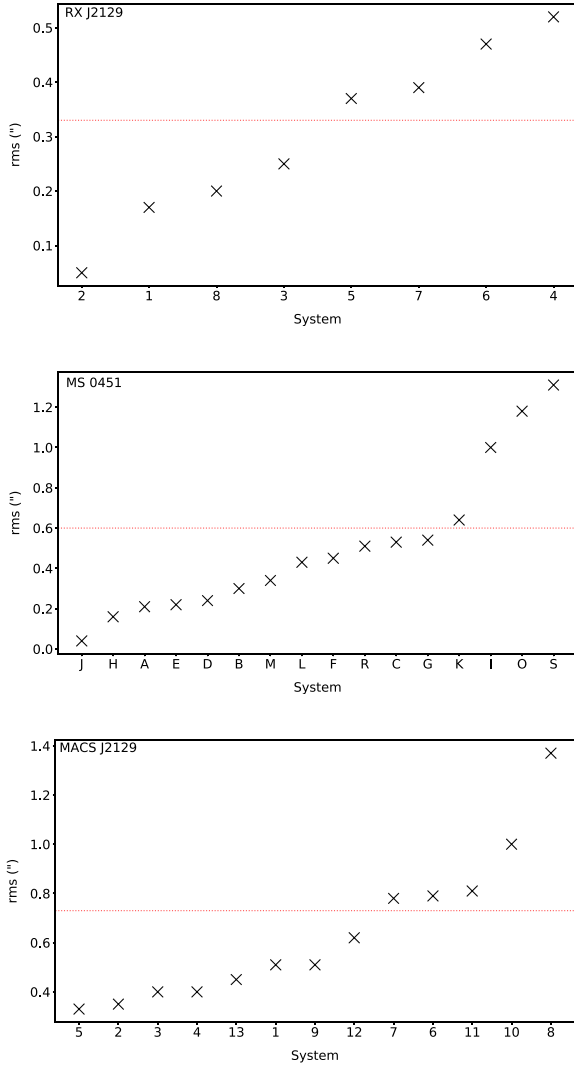
Figure 7. *Left:* RMS for each multiple image system in RX J2129 (top), MS 0451 (middle), and MACS J2129 (bottom). The red dashed line shows the rms of the best-fitting mass model. *Right:* Optimized potentials displayed on a composite colour image using *HST* images in the F475W, F814W, F160W pass-bands for RX J2129 (top) and MACS J2129 (bottom), and in the F814W, F110W, F160W pass-bands for MS 0451 (middle).

We measure an Einstein radius of $\theta_E = (19 \pm 2)$ arcsec for a source redshift $z = 2.0$. This is higher than previous measurements presented by Richard et al. (2010) and Zitrin et al. (2015), $\theta_{E, Richard+10} = (9.0 \pm 1.4)$ arcsec and $\theta_{E, Zitrin+15} = 13$ arcsec. In terms of total mass, we measure $M(R < 250\,\text{kpc}) = (1.49 \pm 0.04) \times 10^{14}\,M_\odot$, which is in good agreement with the measurement given by Richard et al. (2010) of $M_{Richard+10}(R < 250\,\text{kpc}) = (1.37 \pm 0.37) \times 10^{14}\,M_\odot$. Zitrin et al. (2015) quote a mass within 13 arcsec, which corresponds to ~50 kpc at the cluster redshift, $M_{Zitrin+15}(R < 50\,\text{kpc}) = 0.19 \times 10^{14}\,M_\odot$, which is of the same order as what we obtain with our model, $M(R < 50\,\text{kpc}) = (0.17 \pm 0.01) \times 10^{14}\,M_\odot$. Caminha et al. (2019) quote an integrated mass of $M_{Caminha+19}(R < 200\,\text{kpc}) = (1.19 \pm 0.01) \times 10^{14}\,M_\odot$, in excellent agreement with our value of $M(R < 200\,\text{kpc}) = (1.16 \pm 0.03) \times 10^{14}\,M_\odot$. Thanks to discussions with Desprez et al. (2018), we could get the integrated total mass measured with their model within the multiple image region, $M_{Desprez+18}(R < 70\,\text{kpc}) = (0.29 \pm 0.01) \times 10^{14}\,M_\odot$, value which is in good agreement with our measurement presented before. It is important to note that at the time Richard et al. (2010) and Zitrin et al. (2015) published their strong-lensing

mass models, the spectroscopic coverage of RX J2129 was poor. Indeed, only one system, System 1 in this work, had a spectroscopic measurement. Richard et al. (2010) model was only constrained using that system (3 multiple images in total), and Zitrin et al. (2015) model included 6 systems (18 multiple images total) as constraints. In our case, we have 8 systems, 23 multiple images in total as can be seen in Table 5, all spectroscopically confirmed (except System 2 for which we assume the photometric redshift measured by Desprez et al. 2018). This could explain the discrepancies in the measured Einstein radii between these analyses and our model.

4.2 MS 0451

Our best model is constrained by 16 multiple image systems, 5 spectroscopically confirmed, and is composed of 146 haloes including 2 large-scale haloes, and 7 galaxy-scale haloes independently optimized. The best-fitting model has an rms of 0.6 arcsec. In the middle panel of Fig. 8, we compare the density profiles obtained with the *fiducial model* and the new model presented here. The two profiles are in excellent agreement, with a slightly higher density predicted in the

Table 8. Best-fitting parameters of the mass models for all three clusters. Column (1) gives the cluster name. In brackets, we list the rms, the number of degrees of freedom, *dof*, and the number of multiple images respectively for each best-fitting model. Column (2) is the ID of the optimized potential. The IDs of the large-scale haloes are highlighted in bold. Columns (3) to (9) are respectively the R A and Decl. of the center for each halo and subhalo in arcseconds relative to the chosen center as given in Sect. 3, the ellipticity, the orientation angle, the core radius, the truncation radius, and the velocity dispersion for each optimized potentials. The position angle, θ, is given in degrees and is defined as the direction of the semimajor axis of the iso-potential, counted counterclockwise from the horizontal axis (being the R A axis). For each free parameter of the models, we indicate the 1σ error bars computed from the posterior distribution of the MCMC samples. For scaling relations, the reference magnitudes are $\mathrm{mag_{F814W}} = 17.49$, $\mathrm{mag_{F814W}} = 18.69$, and $\mathrm{mag_{F814W}} = 19.19$ for RX J2129, MS 0451, and MACS J2129, respectively. Values in brackets are fixed in the model.

Cluster	ID	R A (arcsec)	Decl. (arcsec)	e	θ (deg)	r_c (kpc)	r_t (kpc)	σ (km s^{-1})
RX J2129	**C1**	3.13 ± 0.77	-1.94 ± 0.41	0.69 ± 0.04	-23.4 ± 0.8	54 ± 6	[1000]	920 ± 21
(0.29 arcsec,	BCG	[0.0]	[0.0]	[0.49]	[-35.4]	[0.3]	64 ± 37	317 ± 25
22, 25)								
	G1	$[-44.2]$	[68.0]	[0.11]	[-50.6]	[0.15]	56^{+5}_{-40}	193^{+2}_{-13}
	L^* galaxy	–	–	–	–	[0.15]	10 ± 5	151 ± 25
MS 0451	**C1**	$-7.5^{+0.9}_{-1.2}$	$-2.6^{+0.6}_{-0.7}$	$0.63^{+0.04}_{-0.03}$	32.2 ± 0.5	121^{+10}_{-7}	[1000]	1101^{+25}_{-34}
(0.60 arcsec,	**C2**	22.3 ± 1.6	19.5 ± 2.2	$0.18^{+0.12}_{-0.06}$	$146.6^{+9.3}_{-15.8}$	332^{+94}_{-30}	685^{+196}_{-75}	811^{+213}_{-68}
18, 47)								
	BCG	[0.0]	[0.0]	[0.6]	[23.7]	[0.19]	17 ± 36	275^{+50}_{-42}
	G1	$[-0.49]$	$[-5.35]$	[0.1]	$[-28.7]$	[0.15]	141 ± 31	341^{+36}_{-33}
	G2	[22.42]	[26.05]	[0.51]	$[-77.2]$	[0.15]	18 ± 46	105^{+38}_{-23}
	G3	$[-29.98]$	$[-17.33]$	[0.62]	[51.7]	[0.15]	147 ± 37	140^{+19}_{-30}
	G4	[11.68]	[23.47]	[0.79]	[34.4]	[0.15]	102 ± 44	45^{+45}_{-22}
	G5	$30.1^{+0.05}_{-0.50}$	$6.6^{+0.2}_{-0.4}$	$0.02^{+0.6}_{-0.01}$	138^{+94}_{-13}	[0.15]	128^{+55}_{-44}	132^{+23}_{-17}
	G6	$[-43.84]$	[0.47]	[0.44]	[53.1]	[0.15]	29 ± 46	55 ± 14
	L^* galaxy	–	–	–	–	[0.15]	68.0 ± 11.5	157 ± 11
MACS J2129	**C1**	$-2.9^{+2.4}_{-0.8}$	$1.2^{+1.1}_{-0.2}$	0.67 ± 0.01	171.6 ± 0.5	96 ± 5	[1000]	1125 ± 20
(0.74 arcsec,	**C2**	$44.6^{+0.01}_{-1.8}$	$17.6^{+0.8}_{-2.5}$	0.79 ± 0.10	59 ± 8	135 ± 43	[1000]	565 ± 4863
33, 42)								
	BCG	$[-0.07]$	[-0.21]	[0.32]	[5.3]	[0.15]	55^{+35}_{-5}	294 ± 42
	G1	$[-2.93]$	[0.81]	[0.44]	[70.0]	[0.15]	44 ± 29	200 ± 33
	G2	[4.53]	$[-1.28]$	[0.27]	$[-31.6]$	[0.15]	43 ± 29	184 ± 36
	G3	[14.42]	[7.24]	[0.47]	[4.6]	[0.15]	7 ± 2	356 ± 48
	G4	[5.92]	[6.84]	[0.39]	[88.5]	[0.15]	85^{+25}_{-18}	201 ± 24
	L^* galaxy	–	–	–	–	[0.15]	50^{+25}_{-19}	164 ± 16

core now, but still within the error bars of the *fiducial model*, which we attribute to the stronger constraints used to optimize our model thanks to the identification of new systems in the north of MS 0451. We measure a total mass within the multiple image region that extends up to ~ 350 kpc, $M(R < 350\,\mathrm{kpc}) = (3.75 \pm 0.11) \times 10^{14}\,\mathrm{M_\odot}$, in good agreement with the value obtained with the *fiducial model*, $M_{\mathrm{fiducial}}(R < 350\,\mathrm{kpc}) = (3.72 \pm 0.03) \times 10^{14}\,\mathrm{M_\odot}$.

We measure an Einstein radius, $\theta_{\mathrm{E}} = (19 \pm 1)$ arcsec, for a source redshift of $z = 2.9$ (i.e. redshift of System A). This value is consistent with the one reported in Zitrin et al. (2011b), $\theta_{\mathrm{E, Zitrin+11}} = (19 \pm 2)''$. We measure an integrated mass within $\theta_{\mathrm{E}} = 120$ kpc of $M(< \theta_{\mathrm{E}}) = (9.15 \pm 0.08) \times 10^{13}\,\mathrm{M_\odot}$. This is slightly higher than what was measured by Zitrin et al. (2011b), $M_{\mathrm{Zitrin+11}}(< \theta_{\mathrm{E}}) = 8.82^{+0.3}_{0.1} \times 10^{13}\,\mathrm{M_\odot}$; however, their mass model only includes 4 systems of multiple images, compared to our analysis which has 16 systems as constraints. Berciano Alba et al. (2010) measured an integrated mass within a radius of 30 arcsec, 188 kpc at the redshift of MS 0451, $M_{\mathrm{BA+09}}(R < 188\,\mathrm{kpc}) = 1.73 \times 10^{14}\,\mathrm{M_\odot}$, which is in excellent agreement with both our measurement, $M(R < 188\,\mathrm{kpc}) = (1.73 \pm 0.02) \times 10^{14}\,\mathrm{M_\odot}$, and the one from Zitrin et al. (2011b) at the same radius, $M_{\mathrm{Zitrin+11}}(R < 188\,\mathrm{kpc}) = 1.80 \times 10^{14}\,\mathrm{M_\odot}$. This strengthens our argument that the difference of mass values between Zitrin et al. (2011b) and our work at smaller radii might be due to the improvement of the mass model due to both an increased number of

multiple images to constrain the inner mass distribution of MS 0451, and the spectroscopic information.

The mass obtained for galaxy G5 appears relatively high (see Fig. 7 and Table 8), considering it is not visible in any of the *HST* images and only detected in the MUSE datacube. It is thus likely to be a low-mass galaxy with a velocity dispersion lower than the best-fitting value measured by our mass model, $\sigma = 132$ km s^{-1}. Moreover, as it is not detected in the *HST* imaging, we do not have any shape measurements for G5. The model thus optimizes all its parameters apart from its core radius, r_c. The best-fitting parameters for this galaxy might be strongly degenerated. It is thus difficult to conclude.

Oppositely, the cluster galaxy G4 is predicted with a velocity dispersion $\sigma = 45$ km s^{-1}, which is likely underestimated given the size of the galaxy (see Fig. 7). This can be explained by the addition of the second large-scale halo in its vicinity, which might induce a non-physical 'mass transfer' between the two haloes. However, as explained in Section 3, this second large-scale halo is necessary to account for the impact of the two galaxy groups in this region, and without which we cannot recover the quintuply imaged system at $z = 6.7$ (Knudsen et al. 2016; Richard et al. in preparation).

The rms of each multiple image is given in Table 6, and the predicted position together with their magnification, μ, of the unidentified counter-images of the systems used as constraints are

given in Table 9, namely System J and System S. Images J.3, S.3, and S.4 are highlighted as cyan circles in Fig. 3. The two systems in the north of the cluster, Systems H and R, are well reproduced, with an rms of 0.16 and 0.51 arcsec, respectively. The same goes for the group of systems located in the vicinity of the giant arc A, south of the cluster, i.e. Systems A, B, C, D, E, F, G, and K). Systems I and O are not as well reproduced as the others, with an rms of 1.0 and 1.18 arcsec, respectively. We explain this by the location of one of their multiple images, Images I.2 and O.2. Image I.2 is located close to a faint cluster galaxy which is not individually optimized, but might act as a small-scale perturber. A mass model that includes the cluster galaxy close to Image I.2 does not show any significant improvements compare to our best model when considering the number of added free parameters. Image O.2 is located in a region which is highly contaminated by the light of the BCG, meaning we could be missing local perturbers.

Moreover, MacKenzie et al. (2014) discussed the group of multiply lensed submilimetric galaxies at $z = 2.9$, corresponding to Systems A, B, C, D, E, F, and G in this work. They provide magnification estimates for each image, in excellent agreement with the magnifications measured with our best model. Table 10 gives the measured magnifications by this analysis as well as the ones measured in MacKenzie et al. (2014). The largest differences are seen for highly magnified images such as Images A.1, A.2, G.2, and G.3. This was to be expected as in high magnification regions such measurements have large uncertainties. Indeed magnification is supposedly infinite on critical lines, making these measurements difficult to believe, apart from the fact that lensed galaxies located in these regions are highly magnified. One more thing to consider is the unambiguous measurement of the redshift of System G with MUSE of $z = 2.93$. Indeed this value differs from the one used in MacKenzie et al. (2014), $z = 3.11 \pm 0.03$, which was initially measured by Takata et al. (2003).

4.2.1 System S

Although spectroscopically confirmed, System S is not well reproduced by the model, with an rms of 1.3 arcsec. Both Images S.1 and S.2 are in the high magnification region of the cluster, close to the radial critical line at the redshift of the source, $z = 4.45$, with a measured magnification for S.1 of $\mu > 300$. System S is predicted to be quadruply imaged. Images S.1 and S.2 are only detected in the MUSE datacube, as their proximity to the BCG makes them undetectable in the *HST* images. Counter-images are predicted further away from the BCG, with relatively low magnifications as quoted in Table 9. That could explain why Image S.3 is not detected in the MUSE datacube, while Image S.4 is predicted outside the MUSE field of view as can be seen in Fig. 3 (cyan circles). However, the lack of photometric identification of Images S.1 and S.2 in the *HST* images makes them impossible to identify as we have no idea of their colour nor morphology.

4.3 MACS J2129

Our best model is constrained by 13 multiple image systems, 12 spectroscopically confirmed, and is composed of 151 haloes including 2 large-scale haloes and 4 galaxy-scale haloes independently optimized. The constraints used in this model are the same as the ones presented in Caminha et al. (2019), except for a newly identified system, System 10, and the removal of System 14, as discussed in Section 3. The best-fitting model has an rms of 0.74 arcsec. The

right-hand panel of Fig. 8 shows the density profiles obtained with this work and our *fiducial model*. One can notice differences between the two density profiles in the very inner region of the cluster, $R < 10$ kpc; however, this discrepancy is difficult to interpret as within this region the density is dominated by the stellar content of the BCG, and thus we lack constraints from strong lensing. At $R > 10$ kpc, the new model exhibits overdensity peaks not visible in the *fiducial model* density profile. This is explained by the inclusion of new constraints in this region, both multiple images and cluster galaxies up to $R \sim 100$ kpc. In terms of total mass within the multiple image region, which extends up to ~ 300 kpc, we measure $M(R < 300$ kpc$) = (2.94 \pm 0.02) \times 10^{14}$ M$_\odot$, in good agreement with the value from the *fiducial model*, $M_{\rm fiducial}(R < 300$ kpc$) = (2.97 \pm 0.02) \times 10^{14}$ M$_\odot$.

The properties of the main dark matter halo (namely, C1 in Table 8) are consistent with those reported in Monna et al. (2017) and Caminha et al. (2019). Our best-fitting model also favours a relatively large core radius, $r_c = (96 \pm 5)$ kpc, in excellent agreement with Monna et al. (2017) measurement of $r_{c, \rm Monna+17} = (101 \pm 13)$ kpc. Caminha et al. (2019), who are also using the LENSTOOL software, quote a core radius for the main cluster-scale halo of $r_{c, \rm Caminha+19} = (74 \pm 4)$ kpc. This is slightly lower than what we obtain. The second cluster-scale halo they include has similar properties to this work (C2 in Table 8); however, their model favours it closer to the BCG, ~ 250 kpc *versus* ~ 320 kpc in this work. This might explain the lower value of r_c for C1 obtained by Caminha et al. (2019) compared to our work. We find that velocity dispersions of the galaxy-scale haloes, BCG, G1, and G2, are overestimated compared to their luminous counterparts. This is explained by the correlation between the baryonic mass distribution within central galaxies, and the size of the core of the dark matter halo (Newman et al. 2013a,b), which was already evidenced by Monna et al. (2017).

We measure an Einstein radius for a source redshift $z = 2.0$ of $\theta_{\rm E} = (23 \pm 2)$ arcsec, which is within the error bars of what Zitrin et al. (2011b, 2015) measured for a similar source redshift, $\theta_{\rm E, Zitrin+11,15} = (19 \pm 2)$ arcsec. Monna et al. (2017) quote an Einstein radius for a source redshift $z = 1.36$, $\theta_{\rm E, Monna+17} = (14 \pm 2)$ arcsec, of similar order to what we measure at the same source redshift, $\theta_{\rm E} = (18 \pm 1)$ arcsec. In order to compare our model with Monna et al. (2017), Zitrin et al. (2011b, 2015), we now quote masses within a radius of 19 arcsec, which corresponds to ~ 130 kpc at the redshift of MACS J2129. We measure a total mass of $M(R < 130$ kpc$) = (1.04 \pm 0.01) \times 10^{14}$ M$_\odot$, slightly higher than what is measured by Monna et al. (2017), $M_{\rm Monna+17}(R < 130$ kpc$) = (0.89 \pm 0.01) \times 10^{14}$ M$_\odot$, but within the error bars of the measurements given by Zitrin et al. (2011b, 2015), $M_{\rm Zitrin+11,15}(R < 130$ kpc$) = 0.92 \pm 0.09 \times 10^{14}$ M$_\odot$. Caminha et al. (2019) quote a mass of $M_{\rm Caminha+19}(R < 200$ kpc$) = (1.84 \pm 0.01) \times 10^{14}$ M$_\odot$, in excellent agreement with our measurement of $M(R < 200$ kpc$) = (1.81 \pm 0.02) \times 10^{14}$ M$_\odot$.

Globally, multiple images are well recovered by our model, except for System 8 which has an rms $= 1.37$ arcsec. The new multiple image system reported in this work, i.e. Systems 10, is well-recovered, with an rms $= 0.61$ arcsec. In particular, we note that the inclusion of the cluster galaxy G3 (see Table 8) is critical for the recovery of this system. The addition of the second cluster-scale halo in the north-east of the cluster significantly improves the recovery of Systems 3 and 6 compared to the model presented by Monna et al. (2017). We measure an rms of 0.40 arcsec, to be compared to ~ 0.8 arcsec for System 3 when G3 is not included, and 0.79 arcsec to be compared to 1.7 arcsec for System 6. While four over the five multiple images of System 8 are spectroscopically confirmed, it has an rms of 1.37 arcsec. We note that the inclusion of galaxy G4 in the model seems to be responsible
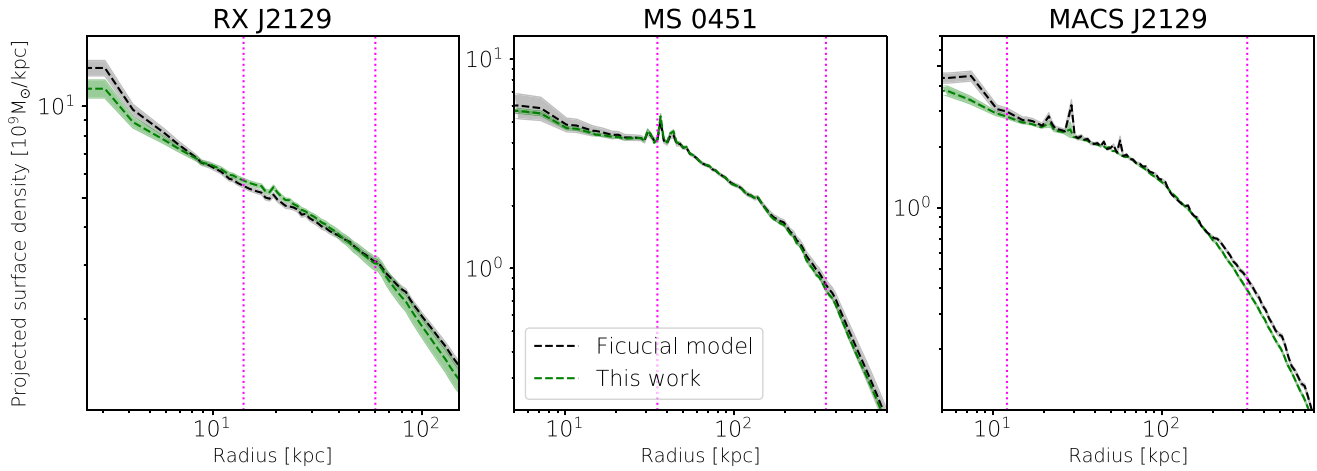
Figure 8. Radial surface density profiles for RX J2129 (left), MS 0451 (middle), and MACS J2129 (right) derived from the strong-lensing mass models described in this work. Measurements from the *fiducial model* are shown in grey, and measurements with our new mass models are shown in green. Fiducial models were built based on the analyses of Caminha et al. (2019) and Monna et al. (2017) for RX J2129 and MACS J2129. In each plot, the dashed line stands for the mean surface density, and the shaded areas indicate the 1σ error bars. The two magenta dashed lines highlight the positions, from the cluster centre, of the closest and most distant multiple image used as constraints for each model.

Table 9. Predicted positions of the unidentified counter images from the best model of MS 0451. Column (1) stands for the identifier of the image with respect to the system it belongs to. Columns (2) and (3) are, respectively, the R A and Decl. in degrees (J2000) of the images. Column (4) gives the measured magnification of the images at their predicted positions. The images are highlighted as cyan circles in Fig. 3.

Image ID	R A [J2000]	Decl. [J2000]	μ
J.3	73.55100	−3.01006	3.5 ± 0.3
S.3	73.54862	−3.01063	13.0 ± 3.0
S.4	73.54093	−3.02420	2.2 ± 0.2

Table 10. Measured magnification for the lensed submillimetric galaxies identified in Borys et al. (2004) and MacKenzie et al. (2014). We list the IDs of the multiple images following Table 6, and add the ID from MacKenzie et al. (2014) in brackets. We here give the magnifications measured from our best model, as well as the ones reported in MacKenzie et al. (2014).

ID	RA [J2000]	Decl. [J2000]	μ	$\mu_{MK + 14}$
A.1/D.1 (7a)	73.55396	−3.01482	>50	33 ± 2
A.2/D.2 (7b)	73.55389	−3.01595	34.2 ± 7.9	45 ± 3
A.3/D.3 (7c)	73.54630	−3.02404	3.0 ± 0.2	2.9 ± 0.1
B.1 (5a)	73.55335	−3.01232	5.4 ± 0.6	5.3 ± 0.1
B.2 (5b)	73.55285	−3.01707	4.9 ± 0.6	6.4 ± 0.1
B.3 (5c)	73.54553	−3.02348	2.9 ± 0.2	2.9 ± 0.1
C.1 (6a)	73.55339	−3.01325	7.4 ± 0.9	8.2 ± 0.2
C.2 (6b)	73.55304	−3.01656	5.3 ± 0.6	5.0 ± 0.1
C.3 (6c)	73.54545	−3.02380	2.7 ± 0.2	2.8 ± 0.1
E.1 (2a)	73.55481	−3.01065	2.9 ± 0.2	2.9 ± 0.1
E.2 (2b)	73.55241	−3.01996	7.2 ± 1.4	8.1 ± 0.4
E.3 (2c)	73.54911	−3.02226	4.9 ± 0.5	6.1 ± 0.1
F.1 (3a)	73.55435	−3.01088	3.0 ± 0.2	3.2 ± 0.1
F.2 (3b)	73.55282	−3.01918	3.3 ± 0.3	3.0 ± 0.1
F.3 (3c)	73.54775	−3.02268	3.3 ± 0.3	4.3 ± 0.1
G.1 (1a)	73.55593	−3.01193	3.8 ± 0.3	3.8 ± 0.1
G.2 (1b)	73.55271	−3.02124	10.9 ± 2.1	20 ± 1
G.3 (1c)	73.55071	−3.02261	6.1 ± 0.6	7.3 ± 0.1

for that, as it degrades the accuracy of the reconstruction of System 8 (Image 8.3 is poorly reproduced). However, G4 is necessary to recover precisely Systems 1 and 7, decreasing the rms of the overall model from 0.95 to 0.73 arcsec.

Finally, MACS J2129 also hosts a particularly red and bright single strongly lensed galaxy, West of the cluster centre as shown in Fig. 4 ($\alpha = 322.34311$, $\delta = -7.69203$). Toft et al. (2017) presented a detailed analysis of this $z = 2.1472$ compact galaxy, spectroscopically confirmed thanks to VLT/X-Shooter observations, and which revealed to be a fast-spinning, rotationally supported disc galaxy. Thanks to their lensing mass model, Toft et al. (2017) measured a magnification of $\mu_{Toft + 17} = 4.2 \pm 0.6$. While this galaxy is not used in the mass model presented here as it is singly imaged, we can measure its predicted magnification. We measure $\mu = 3.7 \pm 0.2$, a slightly lower value than the one from Toft et al. (2017), but in good agreement within error bars. One should note that their strong-lensing mass model was only constrained by two multiple image systems, namely Systems 1 and 3 in Table 7.

5 SUMMARY AND CONCLUSIONS

In this paper, we present new strong-lensing mass models for three galaxy clusters, MS 0451, MACS J2129, and RX J2129, which include new VLT/MUSE observations. We combine the MUSE datacubes with high-resolution imaging from *HST* available for each cluster to maximize the number of extracted spectra. We measure the redshift of each source with a dedicated software, IFS-REDEX (Rexroth et al. 2017), allowing for a wavelet-based filtration of the spectra. Our conclusions are as follows:

(i) We measure 158, 171, and 189 secured or likely spectroscopic redshifts in the RX J2129, MS 0451, and MACS J2129 MUSE datacubes, respectively. For MS 0451, we identify two new systems of multiple images located in the north of the cluster core, the least constrained region, confirm the redshift of System A measured by Borys et al. (2004), and measure the redshift of the three multiple images of System G. For RX J2129 and MACS J2129, we obtain measurements in excellent agreement with Caminha et al. (2019).

We report a new multiple image system detection, System 10 at $z = 4.41$, in MACS J2129. Finally, the MUSE datacubes allowed us to spectroscopically confirm 43, 112, and 89 cluster members in RX J2129, MS 0451, and MACS J2129, respectively. Among those, in RX J2129 and MACS J2129, 15 and 4 cluster members, respectively, are new identifications, i.e. not reported by Caminha et al. (2019).

(ii) We carried out a fruitful blind search while combining *HST* imaging with MUSE datacubes using MUSELET. It played a decisive role in the identification of multiple image systems, since it highlighted strong emission lines invisible in the *HST* images due to either the faintness of the sources at wavelengths not corresponding to maximum emissions, or their proximity to luminous emitters in the foreground. This was particularly interesting for MS 0451 where the blind search revealed Systems R and S, both located in the north of the cluster, which before this analysis was lacking strong-lensing constraints.

(iii) Our models are optimized using the parametric version of the LENSTOOL algorithm (Jullo et al. 2007). The multiple image systems in the three clusters were reproduced with an rms of 0.28, 0.6, and 0.74 arcsec in RX J2129, MS 0451, and MACS J2129, respectively. We measure integrated aperture masses in good agreement or within the error bars of the ones published in previous analyses (Berciano Alba et al. 2010; Richard et al. 2010; Zitrin et al. 2011b; Zitrin et al. 2015; Monna et al. 2017; Desprez et al. 2018; Caminha et al. 2019).

(iv) The addition of a second cluster-scale halo in MS 0451 and MACS J2129 mass models are necessary to minimize the rms of the two models, and to recover the multiple image systems geometry in the north and north-east of the two clusters, respectively. Caminha et al. (2019) presented a similar mass model for MACS J2129, with their second cluster-scale halo located in the same region as us, slightly closer to the BCG than in our case, $\sim$250 kpc away from the BCG compared to $\sim$320 kpc in our case. Similarly, the addition of some cluster galaxies located in the vicinity of multiple images played a decisive role in the reconstruction of the mass distribution, e.g. the rms of MACS J2129 improved from 0.95 to 0.74 arcsec just by the addition of G4.

(v) We compare our magnification measurements of the sub-millimetric galaxy group multiply lensed by MS 0451, at $z = 2.91$, with the results published by MacKenzie et al. (2014). The two analyses show excellent agreement, with some differences for the most highly magnified images. This was to be expected as magnification measurements close to the critical line, mathematically a region where magnification is supposed to be infinite, have high uncertainties.

(vi) Our mass model of MACS J2129 allowed us to measure the magnification of the singly imaged $z = 2.1472$ galaxy identified by Toft et al. (2017), $\mu = 3.7 \pm 0.2$. This values is within the error bars of the initial measurement from Toft et al. (2017), $\mu_{Toft+17} = 4.2 \pm 0.6$, which was derived using a mass model only constrained by two systems of multiple images, namely Systems 1 and 3 from our analysis.

(vii) Further investigations have to be carried out to identify the missing counter-images presented in Table 9, and confirm System P in MS 0451. Moreover, we identify a group of galaxies at $z = 0.06$ in MS 0451 that impacts the multiple image geometry, strengthening the need to properly implement multiplane optimization in LENSTOOL.

More generally, our analysis highlights again the power of MUSE to secure and identify strong-lensing features in cluster cores. Such observations are mandatory to recover precisely and accurately the mass distribution in cluster cores. Without such lensing mass models, cluster lenses cannot be used efficiently as gravitational telescopes, as the mass distribution needs to be known in order to recover the intrinsic physical properties of the lensed galaxies (Vanzella et al. 2017; Patrício et al. 2016; Toft et al. 2017; Johnson et al. 2017; Claeyssens et al. 2019). Moreover, the physics in place in clusters themselves is highly dependent on how well we can recover their mass distribution. Indeed, while a multiwavelength analysis is needed to observe all their components (stars and gas), only gravitational lensing gives us an estimate of their total mass, and thus indirectly of their dark matter content and distribution. With such knowledge, we can hope to use galaxy clusters as probes of the nature of dark matter (Jauzac et al. 2016b, 2018; Robertson et al. 2019).

DATA AVAILABILITY

The data underlying this article will be shared on reasonable request to the corresponding author.

REFERENCES

Acebron A., Jullo E., Limousin M., Tilquin A., Giocoli C., Jauzac M., Mahler G., Richard J., 2017, MNRAS, 470, 1809

Atek H. et al., 2015, ApJ, 814, 69

Atek H., Richard J., Kneib J.-P., Schaerer D., 2018, MNRAS, 479, 5184

Bacon R. et al., 2010, in McLean I. S., Ramsay S., Takami H., eds, Ground-based and Airborne Instrumentation for Astronomy III. Vol. 7735, SPIE, p. 773508

Bacon R. et al., 2015, A&A, 575, A75

Bacon R., Piqueras L., Conseil S., Richard J., Shepherd M., 2016, Astrophysics Source Code Library, record ascl:1611.003

Bacon R. et al., 2017, A&A, 608, A1

Bartelmann M., Maturi M., 2017, Scholarpedia, 12, 32440

Belli S., Jones T., Ellis R. S., Richard J., 2013, ApJ, 772, 141

Berciano Alba A., Garrett M. A., Koopmans L. V. E., Wucknitz O., 2007, A&A, 462, 903

Berciano Alba A., Koopmans L. V. E., Garrett M. A., Wucknitz O., Limousin M., 2010, A&A, 509, A54

Bertin E., Arnouts S., 1996, A&AS, 117, 393

Borys C. et al., 2004, MNRAS, 352, 759

Bouwens R. J., Oesch P. A., Illingworth G. D., Ellis R. S., Stefanon M., 2017, ApJ, 843, 129

Caminha G. B. et al., 2017a, A&A, 600, A90

Caminha G. B. et al., 2017b, A&A, 607, A93

Caminha G. B. et al., 2019, A&A, 632, A36

Cerny C. et al., 2018, ApJ, 859, 159

Chirivì G., Suyu S. H., Grillo C., Halkola A., Balestra I., Caminha G. B., Mercurio A., Rosati P., 2018, A&A, 614, A8

Claeyssens A. et al., 2019, MNRAS, 489, 5022

Coe D., Bradley L., Zitrin A., 2015, ApJ, 800, 84

Covone G., Kneib J.-P., Soucail G., Richard J., Jullo E., Ebeling H., 2006, A&A, 456, 409

Desprez G., Richard J., Jauzac M., Martinez J., Siana B., Clément B., 2018, MNRAS, 479, 2630

Diego J. M., Broadhurst T., Wong J., Silk J., Lim J., Zheng W., Lam D., Ford H., 2016, MNRAS, 459, 3447

Diego J. M. et al., 2018, ApJ, 857, 25

Donahue M., Gaskin J. A., Patel S. K., Joy M., Clowe D., Hughes J. P., 2003, ApJ, 598, 190

Ebeling H., Barrett E., Donovan D., Ma C.-J., Edge A. C., van Speybroeck L., 2007, ApJ, 661, L33

Elíasdóttir Á. et al., 2007, preprint (arXiv:0710.5636)

Ellingson E., Yee H. K. C., Abraham R. G., Morris S. L., Carlberg R. G., 1998, ApJS, 116, 247

Faber S. M., Jackson R. E., 1976, ApJ, 204, 668

Ford H. C. et al., 2003, in Blades J. C., Siegmund O. H. W., eds, Proc. SPIE Conf. Ser. Vol. 4854, Future EUV/UV and Visible Space Astrophysics Missions and Instrumentation. SPIE, Bellingham, p. 81

Geach J. E. et al., 2006, ApJ, 649, 661

Gioia I. M., Maccacaro T., Schild R. E., Wolter A., Stocke J. T., Morris S. L., Henry J. P., 1990, ApJS, 72, 567

Grillo C., 2016, ApJ, 822, 78

Harvey D. et al., 2014, MNRAS, 441, 404

Harvey D., Massey R., Kitching T., Taylor A., Tittley E., 2015, Science, 347, 1462

Harvey D., Kneib J. P., Jauzac M., 2016, MNRAS, 458, 660

Hoekstra H., Bartelmann M., Dahle H., Israel H., Limousin M., Meneghetti M., 2013, Space Sci. Rev., 177, 75

Huang K.-H. et al., 2016, ApJ, 823, L14

Ishigaki M., Kawamata R., Ouchi M., Oguri M., Shimasaku K., Ono Y., 2018, ApJ, 854, 73

Jauzac M. et al., 2014, MNRAS, 443, 1549

Jauzac M. et al., 2015, MNRAS, 446, 4132

Jauzac M. et al., 2016a, MNRAS, 457, 2029

Jauzac M. et al., 2016b, MNRAS, 463, 3876

Jauzac M. et al., 2018, MNRAS, 481, 2901

Jauzac M. et al., 2019, MNRAS, 483, 3082

Johnson T. L., Sharon K., 2016, ApJ, 832, 82

Johnson T. L., Sharon K., Bayliss M. B., Gladders M. D., Coe D., Ebeling H., 2014, ApJ, 797, 48

Johnson T. L. et al., 2017, ApJ, 843, L21

Joye W. A., Mandel E., 2003, in Payne H. E., Jedrzejewski R. I., Hook R. N., eds, ASP Conf. Ser. Vol. 295, Astronomical Data Analysis Software and Systems XII. Astron. Soc. Pac., San Francisco, p. 489

Jullo E., Kneib J.-P., Limousin M., Elíasdóttir Á., Marshall P. J., Verdugo T., 2007, New J. Phys., 9, 447

Jullo E., Natarajan P., Kneib J.-P., D'Aloisio A., Limousin M., Richard J., Schimd C., 2010a, Science, 329, 924

Jullo E., Natarajan P., Kneib J. P., D'Aloisio A., Limousin M., Richard J., Schimd C., 2010b, Science, 329, 924

Kassiola A., Kovner I., 1993, ApJ, 417, 450

Kilbinger M., 2015, Rep. Progr. Phys., 78, 086901

Kneib J.-P., Natarajan P., 2011, A&AR, 19, 47

Kneib J.-P., Ellis R. S., Smail I., Couch W. J., Sharples R. M., 1996, ApJ, 471, 643

Knudsen K. K., Richard J., Kneib J.-P., Jauzac M., Clément B., Drouart G., Egami E., Lindroos L., 2016, MNRAS, 462, L6

Lagattuta D. J. et al., 2017, MNRAS, 469, 3946

Lagattuta D. J. et al., 2019, MNRAS, 485, 3738

LaRoque S. J. et al., 2003, ApJ, 583, 559

Limousin M., Kneib J.-P., Natarajan P., 2005, MNRAS, 356, 309

Limousin M. et al., 2007, ApJ, 668, 643

Livermore R. C., Finkelstein S. L., Lotz J. M., 2017, ApJ, 835, 113

Lotz J. M. et al., 2017, ApJ, 837, 97

MacKenzie T. P. et al., 2014, MNRAS, 445, 201

Mahler G. et al., 2018, MNRAS, 473, 663

Mahler G. et al., 2019, ApJ, 873, 96

Ma C.-J., Ebeling H., Donovan D., Barrett E., 2008, ApJ, 684, 160

Massey R., Kitching T., Richard J., 2010, Rep. Progr. Phys., 73, 086901

Molnar S. M., Hughes J. P., Donahue M., Joy M., 2002, ApJ, 573, L91

Monna A. et al., 2017, MNRAS, 466, 4094

Natarajan P., Kneib J.-P., 1997, MNRAS, 287, 833

Natarajan P. et al., 2017, MNRAS, 468, 1962

Newman A. B., Treu T., Ellis R. S., Sand D. J., Nipoti C., Richard J., Jullo E., 2013a, ApJ, 765, 24

Newman A. B., Treu T., Ellis R. S., Sand D. J., 2013b, ApJ, 765, 25

Niemiec A., Jauzac M., Jullo E., Limousin M., Sharon K., Kneib J.-P., Natarajan P., Richard J., 2020, MNRAS, 493, 3331

Patrício V. et al., 2016, MNRAS, 456, 4191

Postman M. et al., 2012, ApJS, 199, 25

Remolina González J. D., Sharon K., Mahler G., 2018, ApJ, 863, 60

Rescigno U. et al., 2020, A&A, 635, A98

Rexroth M., Kneib J.-P., Joseph R., Richard J., Her R., 2017, preprint (arXiv:1703.09239)

Richard J. et al., 2010, MNRAS, 404, 325

Richard J. et al., 2014, MNRAS, 444, 268

Richard J. et al., 2015, MNRAS, 446, L16

Richard J. et al., 2021, A&A, 646, A83

Robertson A., Harvey D., Massey R., Eke V., McCarthy I. G., Jauzac M., Li B., Schaye J., 2019, MNRAS, 488, 3646

Rosati P. et al., 2014, Messenger, 158, 48

Schmidt K. B. et al., 2014, ApJ, 782, L36

Sharon K. et al., 2020, ApJS, 247, 12

Soto K. T., Lilly S. J., Bacon R., Richard J., Conseil S., 2016, MNRAS, 458, 3210

Steinhardt C. L. et al., 2020, ApJS, 247, 64

Takata T. et al., 2003, PASJ, 55, 789

Tam S.-I. et al., 2020, MNRAS, 496, 4032

Toft S. et al., 2017, Nature, 546, 510

Treu T., Ellis R. S., 2015, Contemporary Phys., 56, 17

Treu T. et al., 2015, ApJ, 812, 114

Vanzella E. et al., 2017, MNRAS, 465, 3803

Weilbacher P. M., Streicher O., Urrutia T., Jarno A., Pécontal-Rousset A., Bacon R., Böhm P., 2020, A&A, 641, A28

Weilbacher P. M., Streicher O., Urrutia T., Pécontal-Rousset A., Jarno A., Bacon R., 2014, in Manset N., Forshay P., eds, ASP Conf. Ser. Vol. 485, Astronomical Data Analysis Software and Systems XXIII. Astron. Soc. Pac., San Francisco, p. 451

Williams P. R. et al., 2018, MNRAS, 477, L70

Wittman D., Golovich N., Dawson W. A., 2018, ApJ, 869, 104

Zitrin A., Broadhurst T., Barkana R., Rephaeli Y., Benítez N., 2011a, MNRAS, 410, 1939

Zitrin A. et al., 2011b, ApJ, 742, 117

Zitrin A. et al., 2015, ApJ, 801, 44

SUPPORTING INFORMATION

Supplementary data are available at *MNRAS* online.

Table A1. List of redshifts measured with a quality flag larger than 2 in RX J2129.
Table A2. List of spectroscopically confirmed redshifts in MS 0451.
Table A3. List of measured redshifts in MACS J2129.

Please note: Oxford University Press is not responsible for the content or functionality of any supporting materials supplied by the authors. Any queries (other than missing material) should be directed to the corresponding author for the article.

APPENDIX A: LIST OF SECURE AND LIKELY REDSHIFTS EXTRACTED FROM THE MUSE DATACUBES

We here give the redshifts extracted with a quality flag greater than 2 (i.e. secure or likely) from the MUSE datacubes in Tables A1–A3 for RX J2129, MS 0451, and MACS J2129, respectively.

Table A1. List of redshifts measured with a quality flag larger than 2 in RX J2129. Column (1) is the ID of the source ('sing' and 'cont' stand for singular and continuum emission line in the MUSELET catalogue). If it exists, the index stands for the pointing's number. Columns (2) and (3) are the RA and the Dec. in degrees (J2000). Column (4) is the redshift of the source, and column (5) is the systematic error on the redshift. Column (6) is the QF of the determination. Full table is available as online material.

ID	R A	Decl.	z	z_{err} ($\times 10^{-4}$)	QF
964	322.42145	0.09219	0.0	0.37	3
971	322.42834	0.09236	0.0	1.47	3
927	322.43222	0.09100	0.0	2.19	3
937	322.43228	0.09141	0.0	0.36	3
829	322.42813	0.08774	0.0	1.62	3
[...]					

Table A2. List of spectroscopically confirmed redshifts in MS 0451. The columns are the same as in Table A1. Full table is available as online material.

ID	R A	Decl.	z	z_{err} ($\times 10^{-4}$)	QF
1878	73.537475	−3.00266	−0.0001	0.14	3
1192	73.547325	−3.01903	0.0011	0.18	3
1305	73.546982	−3.01852	0.0023	0.13	3
1321	73.552307	−3.01785	0.0036	0.85	2
1194	73.545318	−3.01586	0.0625	0.08	3
[...]					

Table A3. List of measured redshifts in MACS J2129. The column are the same as in Table A1. Full table is available as online material.

ID	RA	Decl.	z	z_{err} ($\times 10^{-4}$)	QF
1387	322.35269	−7.69278	−0.0001	0.64	3
1706	322.37128	−7.68706	−0.0002	1.05	3
1763	322.34305	−7.68218	−0.0005	0.08	3
1335	322.35529	−7.69425	−0.0007	0.52	3
1691	322.35846	−7.68730	−0.0011	0.18	3
[...]					

APPENDIX B: MULTIPLE IMAGE SYSTEMS WITH MUSE SPECTROSCOPY

We here provide the MUSE spectra of the newly identified multiple image systems in MS 0451, System R and S, and display each system on a composite colour *HST* stamp in Fig. B1. We provide similar information for System G in Fig. B2. We refer the reader to Caminha et al. (2019) for RX J2129 and MACS J2129.
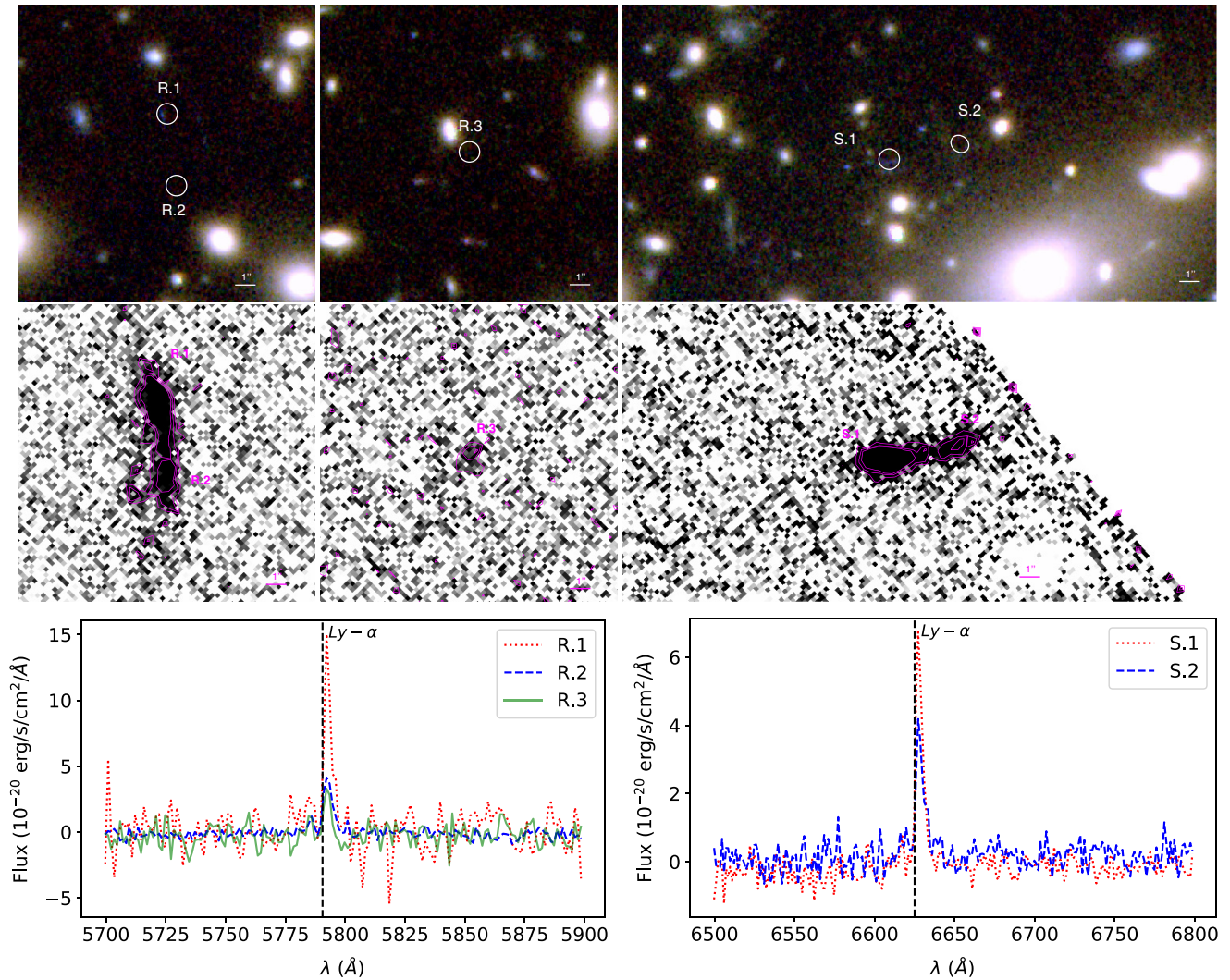
Figure B1. MS 0451 – Newly identified multiple image systems with MUSE. *Top:* Systems R (left, $z = 3.7645$) and S (right, $z = 4.4514$) on a composite colour *HST* image. *Middle:* MUSELET narrow-band datacube at the wavelength corresponding to the maximum emission of the source, i.e. $\lambda = 5793$ Å for System R (left) and $\lambda = 6628$ Å for System S (right). Magenta contours are computed at intensities of 2.0, 3.0, and 4.0×10^{-20} erg s^{-1} cm^{-2} for both systems, except for image R.3, where the contours are computed for an intensity of 1.0×10^{-20} erg s^{-1} arcsec^{-2}. *Bottom:* MUSE spectra of the multiple images centred on the most prominent line.
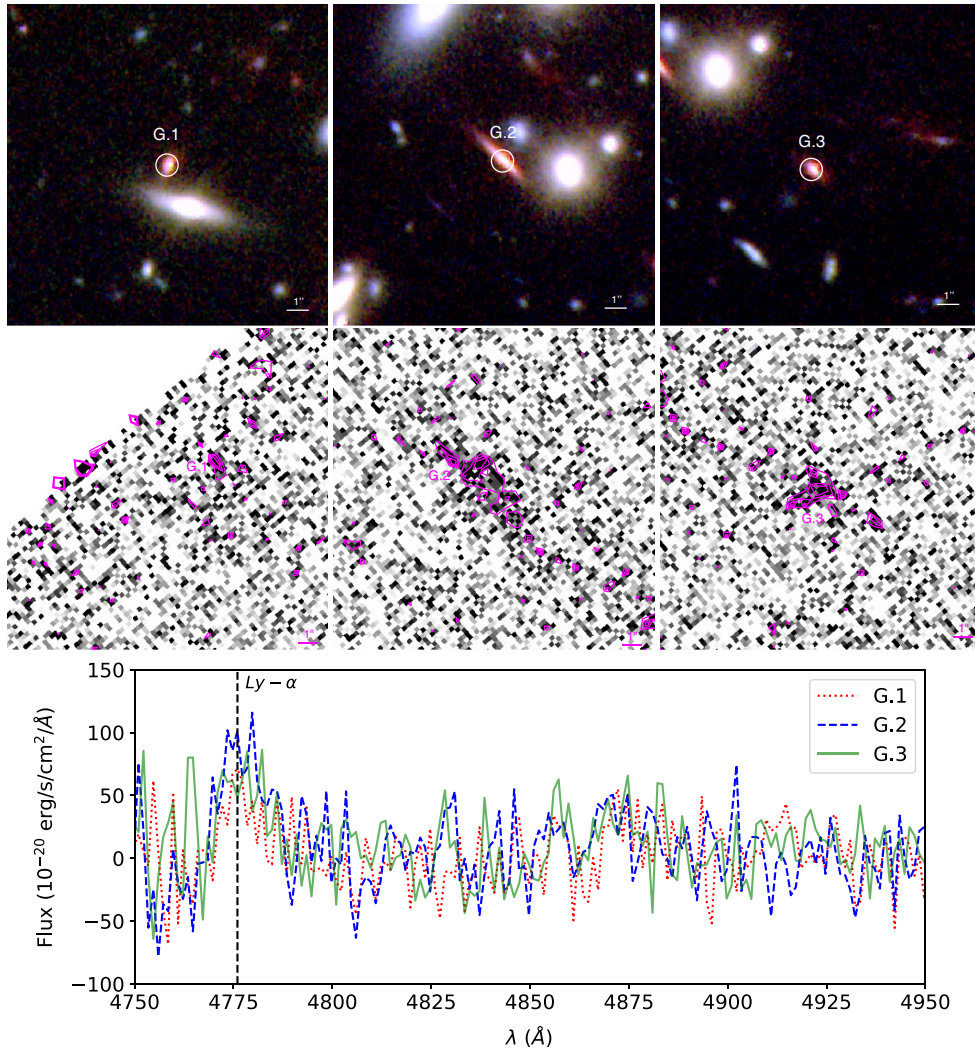
Figure B2. **MS 0451** – System G ($z = 2.93$) identified by Takata et al. (2003), and spectroscopically confirmed with MUSE. *Top:* Composite colour *HST* images. *Middle:* MUSELET narrow-band datacube stamp at the wavelength of the maximum emission of the source, i.e. $\lambda = 4780\,\text{Å}$. The contours are displayed in magenta for 2, 3, and $4 \times 10^{-20}\,\text{erg s}^{-1}\,\text{arcsec}^{-2}$. *Bottom:* MUSE extracted spectra of the multiple images.

This paper has been typeset from a TEX/LATEX file prepared by the author.